J. Fluid Mech. (2007), *vol.* 582, *pp.* 103–132.
doi:10.1017/S0022112007005988 Printed in the United Kingdom

Evolution and mixing of asymmetric Holmboe instabilities

J. R. CARPENTER[1], G. A. LAWRENCE[1] AND W. D. SMYTH[2]

[1]Department of Civil Engineering, University of British Columbia, Vancouver, BC V6T 1Z4, Canada

[2]College of Oceanic and Atmospheric Sciences, Oregon State University, Corvallis, OR 97331, USA

(Received 19 December 2005 and in revised form 23 January 2007)

When a stably stratified density interface is embedded in a region of strong velocity shear, hydrodynamic instabilities result. Here we generalize the stratified shear layer to allow an offset between the centre of the shear layer and the density interface. By including this asymmetry, and keeping the density interface thin with respect to the shear layer, the asymmetric Holmboe (AH) instability emerges. This study examines the evolution and mixing behaviour of AH instabilities, and compares the results to the well-known Kelvin–Helmholtz (KH) and Holmboe instabilities. This is done by performing a series of direct numerical simulations (DNS). The simulation results show that there are two different mixing mechanisms present. The first is a feature of KH instabilities and leads to the mixing and production of intermediate density fluid. The second mixing mechanism is found in AH and Holmboe instabilities and consists of regions of mixing and turbulence production that are located on one or both sides of the density interface. Since the Holmboe-type instabilities do not generate a large-scale overturning of the central isopycnal, the density interface is able to retain its identity throughout the mixing event. The amount of mixing that takes place is found to be strongly dependent on the degree of asymmetry in the flow.

1. Introduction

Many flows of a geophysical and engineering nature involve the horizontal shearing of a stably stratified density interface. Under certain conditions, this flow will become unstable and develop hydrodynamic instabilities. These instabilities are responsible for leading the flow to a turbulent state whereby irreversible mixing of the density field is accomplished. The exact form that these instabilities take – and hence, the evolution of the flow – is dependent on a number of parameters describing the initial velocity and density distributions.

Studies to date have predominantly focused on the case in which the centre of the shear layer and the density interface coincide – referred to herein as the symmetric case. In this case, two different instabilities are possible depending upon the relative strength of the stratification (as measured by an appropriate Richardson number) and the thickness of the density interface. When levels of stratification are sufficiently weak, and conditions for instability are met (to be discussed in the following section), the Kelvin–Helmholtz (KH) instability results. The KH instability is characterized by a periodic roll-up of the density interface caused by the concentration of shear-layer vorticity into discrete billows. The instability has the appearance of a stationary

breaking wave in which the density interface curls up to form statically unstable regions that move with the mean velocity of the flow. The unstable regions of the billow continue to roll up until a saturated amplitude is reached. During this phase of essentially two-dimensional development, secondary instabilities begin to grow. As the billow becomes saturated, the interaction of the secondary instabilities leads the flow into a turbulent collapse, after which a relaminarization occurs (Caulfield & Peltier 2000; Peltier & Caulfield 2003).

As the level of stratification is increased, and the density interface is kept relatively thin in comparison to the shear-layer thickness, the shear is no longer able to overturn the density interface and Holmboe instability develops (Holmboe 1962). Holmboe instability is thought to be the result of a resonant interaction between disturbances in the shear-layer vorticity and internal gravity waves on the density interface (Baines & Mitsudera 1994). Since the density gradient is sufficiently strong and thin, it can be thought of as dividing the shear-layer vorticity into two segments that have only a limited interaction with one another. For this reason, instability develops on each side of the density interface, and is characterized by cusp-like waves that travel at equal and opposite speeds with respect to the mean flow. Each of these unstable waves is referred to as a Holmboe mode.

When asymmetry is introduced (i.e. the velocity and density profiles are offset from one another), and the density interface remains thin, linear theory suggests that one of the two unstable Holmboe modes become preferentially destabilized while the other is more strongly stabilized (Lawrence, Browand & Redekopp 1991). This causes the phenomenon of 'one-sidedness', where disturbances and mixing are found to occur on predominantly one side of the density interface. The occurrence of one-sided flows has been noted in the tilting tube experiments of Thorpe (1968), as well as mixing-layer experiments discussed in Maxworthy & Browand (1975) and Lawrence *et al.* (1991). In the case of mixing-layer experiments, the asymmetry was found to be caused by the different boundary-layer thicknesses between the high- and low-speed layers (Lawrence, Haigh & Zhu 1998). This results in a greater fraction of the shear-layer vorticity in the high-speed layer, and a one-sidedness in the development of the instabilities.

The first laboratory experiments that appeared to confirm the existence of instabilities other than KH in a stratified shear flow were those of Thorpe (1968). Using a tilting tube, Thorpe was able to create a nearly parallel flow for a short period of time until surges formed at the channel ends reached the centre of the tube. Some of the best known photographs of KH billows were taken from these experiments. In addition to KH instabilities, observations were also made of instabilities exhibiting a one-sided behaviour. These appeared as cusp-like waves that travelled with respect to the mean flow. Since the Holmboe instability is predicted to be comprised of both left- and right-propagating modes, these instabilities do not appear to be of the type Holmboe (1962) predicted (though they resemble his predictions in many other respects). Thorpe (1968) notes that throughout the evolution of these one-sided instabilities, the density interface 'retains its identity', presumably meaning that the mixing processes leave the interface relatively intact. In this respect, the mixing is different from that present in KH instabilities, where it is accomplished by a large-scale overturning of the central isopycnal and subsequent mixing of the interface.

In addition to mixing-layer facilities and tilting-tube experiments, the effects of asymmetry have been observed in a number of flows of considerable oceanographic importance. Most notably, in the exchange flow that occurs over the Camarinal Sill in the Strait of Gibraltar (Armi & Farmer 1988). Here, high-salinity water from the

Mediterranean Sea meets lower-salinity Atlantic water, and a bi-directional exchange flow is set up in which an asymmetry is observed in the measured velocity and density profiles. Using acoustic imaging techniques, the asymmetrical instabilities observed were noted to more closely resemble the Holmboe type than symmetrical KH. The presence of turbulence and mixing in flows of this nature has been found to significantly alter their dynamics (e.g. Winters & Seim 2000; Ivey 2004).

One-sidedness is also a common feature in the dynamics of stratified rivers, where dense salt water meets the lighter fresh water from the river discharge. This is known to be the case from studies of salt-wedge intrusions by Sargent & Jirka (1987), Yonemitsu *et al.* (1996) and Yoshida *et al.* (1998). In the latter of these studies, a one-sided overturn was observed using acoustic imaging in the Ishikari River. The overturn is expected to be the result of asymmetry in the velocity and density distributions as well as asymmetrically placed upper and lower boundaries.

Asymmetric density stratified shear instability constitutes a largely unexplored area in the study of mixing in shear flows. To date, the majority of studies have focused on stratified free shear layers subject to the KH instability (e.g. Thorpe 1973; Scinocca 1995; Caulfield & Peltier 1994, 2000; Cortesi, Yadigaroglu & Bannerjee 1998; Smyth 1999; Smyth & Moum 2000*a*, *b*; Staquet 2000; Smyth, Moum & Caldwell 2001; Peltier & Caulfield 2003). This probably stems from the long-standing belief that the KH instability is the only shear instability to develop a large-scale overturning of the density interface (taken as the central isopycnal), thereby precluding other instabilities as a significant source of mixing (Thorpe 1987). However, the findings of Smyth & Winters (2003, after herein referred to as SW03) indicate that in certain regions of parameter space the Holmboe instability, if given enough time, is able to generate levels of mixing and turbulence that exceed those of the KH instability. The long-term nonlinear evolution and mixing behaviour of asymmetric Holmboe (AH) instabilities have not previously been studied.

In this study, the results of SW03 are extended to the asymmetric case, where the evolution and mixing behaviour are examined for a range of asymmetries. This is done through a series of direct numerical simulations. The paper is organized as follows. Section 2 describes relevant parameters, stability characteristics, and the framework by which the evolution of the flow is studied. Section 3 focuses on details of the numerical solution method used. This is followed by a description of the simulation results in § 4, a discussion in § 5, and conclusions in § 6.

2. Background

2.1. *Relevant parameters*

The basic components of a density stratified shear layer consist of initial velocity and density profiles whose variation in the vertical will be represented by hyperbolic tangent functions. A schematic of these idealized profiles is shown in figure 1. The stable layered density distribution has a total difference in density of $\Delta\rho$, and varies over a length scale η between the two layers. Similarly, the velocity difference between the two streams is represented by Δu, which varies continuously over a length scale h_0. The offset between the centre of the shear layer and the centre of the density interface is denoted by d. From these variables it is possible to define two important dimensionless parameters to the evolution of the flow: the scale ratio, $R = h_0/\eta$; and the asymmetry factor, $a = 2d/h_0$. They measure the relative thickness of the regions of velocity and density variations, and the magnitude of the profile asymmetry,

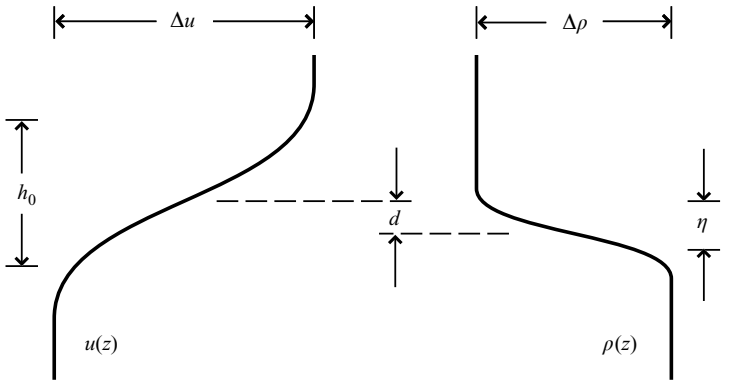

FIGURE 1. Schematic illustrating the parameters considered in the velocity and density distributions of an asymmetric stratified shear layer.

respectively. These profiles are represented mathematically by

$$U(z) = \frac{\Delta u}{2} \tanh\left(\frac{2}{h_0} z - a\right), \tag{2.1a}$$

$$\bar{\rho}(z) = \frac{\Delta \rho}{2} \tanh \frac{2}{h_0} Rz, \tag{2.1b}$$

where the velocity field in a Cartesian coordinate system given by $\boldsymbol{u} = (u, v, w)$ has the initial velocity profile $\boldsymbol{u} = (U(z), 0, 0)$, and the initial density profile $\bar{\rho}(z)$. Here, (x, y, z) denote the streamwise, spanwise and vertical directions, respectively.

Although these profiles are an idealization, the use of hyperbolic tangent profiles was tested experimentally in the laboratory investigation of Yonemitsu *et al.* (1996), where a good agreement was found in the case of salt-wedge intrusions; a flow known to exhibit asymmetry (see § 1).

If we now consider a stratifying agent (usually either heat or salt) with a molecular diffusivity of κ, in a fluid of kinematic viscosity ν, and a reference density of ρ_0, three additional dimensionless parameters result:

$$Re = \frac{\Delta u h_0}{\nu}, \qquad J = \frac{\Delta \rho g h_0}{\rho_0 (\Delta u)^2}, \qquad Pr = \frac{\nu}{\kappa}. \tag{2.2}$$

The Reynolds number, Re, for the simulations discussed in this study is 1200. This value is representative of conditions found in laboratory experiments and may be representative of low-Re mixing events observed in oceans and lakes (Thorpe 1985; Smyth *et al.* 2001). Notably, this Re is within the range of instabilities observed in the seasonal thermocline of the Mediterranean Sea by Woods (1968) (see also Thorpe 1985).

The bulk Richardson number, J, represents the ratio of the stabilizing effect of stratification to the destabilizing effect of the velocity shear, and is chosen to be 0.15. This value of J allows for the growth of both KH and Holmboe instabilities through an adjustment of the scale ratio R, and is representative of conditions found in both field and laboratory studies (Thorpe 1985). The Prandtl number, Pr, is the ratio of the kinematic viscosity to the molecular diffusivity of the stratifying agent, and is therefore a property of the fluid. A value of $Pr = 9$ was chosen for the current simulations, which corresponds to thermal stratification in both fresh and salt water. It should be noted that Pr is also used as a guide in the choice of the initial value

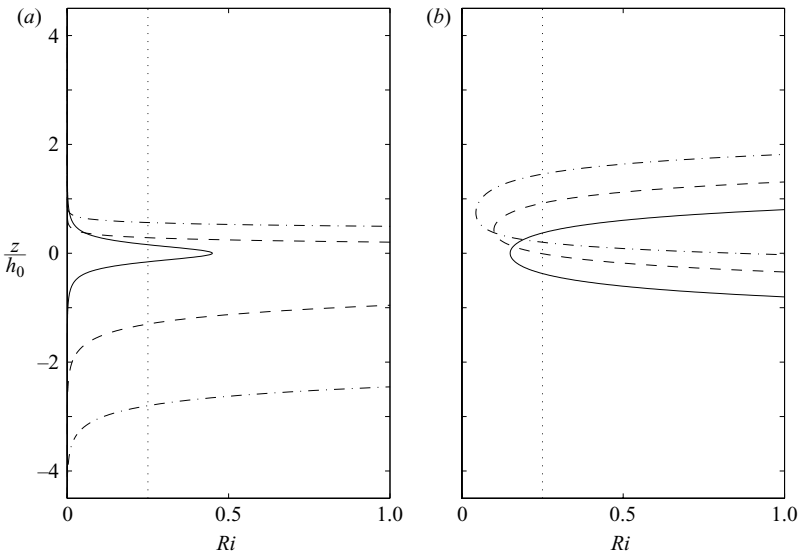

FIGURE 2. Profiles of $Ri(z)$ for the hyperbolic tangent profiles in (2.1) with $J = 0.15$ and $a = 0$ (solid line), $a = 0.5$ (dashed line), and $a = 1.0$ (dot-dashed line). The dotted vertical line indicates $Ri(z) = 0.25$. (*a*) $R = 3$, (*b*) $R = 1$. The centre of the density interface is located at $z/h_0 = 0$ with the shear layer displaced upwards.

of R. This can easily be seen by considering only the process of diffusion acting on both the vorticity of the shear layer, and the stratifying agent of the density interface. Given a time scale τ, each interface will grow by diffusion according to $h_0 \sim (\nu\tau)^{1/2}$ and $\eta \sim (\kappa\tau)^{1/2}$. Taking the ratio of these length scales $R \sim Pr^{1/2}$ is found. Therefore, in most circumstances we will use $R = Pr^{1/2}$.

The choice of R has a large influence on the stability of the flow at $J = 0.15$. This is seen by considering the gradient Richardson number $Ri(z) = N^2/(\mathrm{d}U/\mathrm{d}z)^2$, where $N^2(z) = (g/\rho_0)(-\mathrm{d}\bar{\rho}/\mathrm{d}z)$ is the squared buoyancy frequency. By the Miles–Howard criterion, a necessary condition for instability (based on linear theory of inviscid parallel flow subject to infinitesimal perturbations) is that $Ri(z) < 1/4$ for some z (Miles 1961; Howard 1961). For the hyperbolic tangent profiles used in this study, the choice of $R > 2$ results in the possibility for unstable Holmboe modes to exist in the symmetric ($a = 0$) case (Alexakis 2005). In this case, the regions in which $Ri(z) < 1/4$ are located above and below the centre of the density interface, with $Ri(z)$ attaining a maximum in the region coincident with the density interface (figure 2*a*), expressing the increased stability of this region. A similar $Ri(z)$ profile results when asymmetry is introduced, but the region in the dominant layer displays a slightly larger region of $Ri(z) > 1/4$. For the symmetric case with $R < \sqrt{2}$, there is a $Ri(z)$ minimum in the region of the density interface and the only instability possible is KH (see figure 2*b* for $R = 1$ profiles). If an asymmetry is present in this case, then the region of $Ri(z) < 1/4$ is shifted along with the centre of the shear layer, with a lower minimum value resulting. To our knowledge, asymmetric flows with $R < \sqrt{2}$ have not been examined, and in this study the asymmetry is only applied to the $R = 3$ profiles, where Holmboe modes are predicted (Haigh & Lawrence 1999). It should be noted that the above discussion applies to $J = 0.15$; however, it is possible for the symmetric KH instability to result for $R > \sqrt{2}$ at lower J.

Choice of the parameters mentioned above was also motivated by numerical constraints (to be discussed further in § 3.1) and to facilitate better comparison to the results of SW03.

2.2. *Stability characteristics*

A linear stability analysis of the profiles of (2.1) was first conducted for the symmetric case by Hazel (1972), and subsequently by Smyth, Klaassen & Peltier (1988) and Haigh (1995) where viscosity and mass diffusion were included in the analysis. These studies found that for large enough values of R (Alexakis 2005 found $R > 2$ for inviscid flow) there are two regions of instability: a KH region present when J is sufficiently small, and a Holmboe region for larger J. Across the transition, the solutions of the linear stability problem move from unstable KH modes that are stationary with respect to the mean flow and exhibit higher growth rates, to unstable Holmboe modes that occur in pairs having equal and opposite phase speed and lower growth rates. It should also be noted that in transitioning from the KH region to the Holmboe region there is a rapid change in the wavenumber of the fastest growing mode as well as a rapid decrease in growth rate. It has been confirmed through both numerical simulations (e.g. Smyth *et al.* 1988; SW03) and laboratory experiments (e.g. Maxworthy & Browand 1975) that the KH and Holmboe instabilities have a very different nonlinear appearance. Notably, the KH instability takes the form of a stationary billow, whereas the Holmboe instability consists of two cusp-like propagating waves of equal amplitude and equal but opposite phase speed.

In symmetric flows, the transition between KH and Holmboe instabilities is well defined, and this permits a fairly clear distinction in both the linear and nonlinear regimes between the two. The same is not true in the asymmetric case. Although the nonlinear development of asymmetric stratified shear layers is not well known, both one-sided billowing and cusp-like wave behaviour have been observed (Thorpe 1968; Maxworthy & Browand 1975; Lawrence *et al.* 1991). This has prompted a distinction between 'asymmetric KH' and 'asymmetric Holmboe' instabilities by Lawrence *et al.* (1998) in terms of nonlinear characteristics.

The linear stability properties of asymmetric flows satisfying (2.1) have been studied by Haigh (1995), Haigh & Lawrence (1999) and Lawrence *et al.* (1998), where the region of instability was found to split into two separate and unequal modes that travel in opposite directions. Furthermore, all unstable modes are predicted to possess a non-zero phase speed. In these respects, the resulting instabilities might be considered to be more closely related to the Holmboe instability. However, note that in the limit $a \to \infty$, the resulting instabilities must approach Rayleigh's case of a homogeneous shear layer (Rayleigh 1880).

We plot values of the growth rate σ, phase speed c_r, and wavenumber of maximum growth α_{max}, for each value of the asymmetry considered, where they have been non-dimensionalized by the scales h_0 and Δu (figure 3). This shows a continuous progression from the symmetric Holmboe mode at $a = 0$ to an instability that appears closer to the Rayleigh instability for larger values of a. In light of these results – and the fact that the nonlinear evolution bears a strong resemblance to a Holmboe mode – we have chosen to refer to the instabilities as AH for the remainder of the paper.

2.3. *The partition and transfer of energy*

To gain insight into the processes involved in the evolution of the flow through its various stages of development, it is useful to partition the energy into a number of

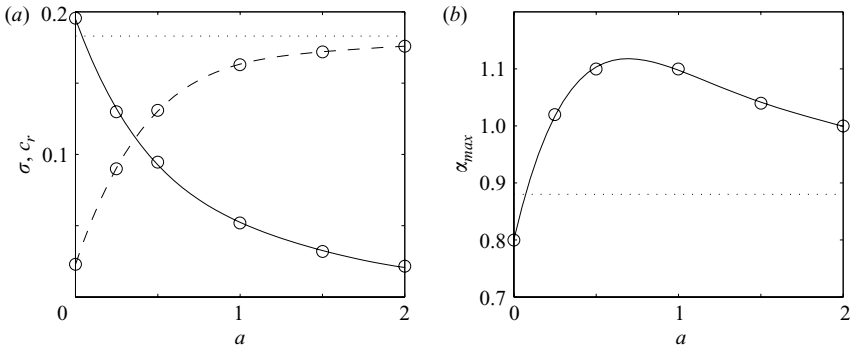

FIGURE 3. Linear stability properties of the unstable mode using profiles (2.1) and the various values of a used in this study (indicated by the circles). (a) The growth rate (dashed line) and the phase speed (solid line). (Note that in the symmetric Holmboe case ($a = 0$) only the positive phase speed is shown.) The horizontal dotted line marks the growth rate of Rayleigh's instability of a homogeneous shear layer, which is stationary and therefore coincident with the a-axis for the case of the c_r curve. (b) The wavenumber of maximum growth is plotted with the dotted line again marking the value of the associated Rayleigh instability. The values presented were obtained from solution to the Taylor–Goldstein equations as discussed in § 3.2 for $J = 0.15$, $Re = 1200$, $Pr = 9$ and $R = 3$.

different reservoirs. As the flow evolves, the energy transfers between these reservoirs are calculated, based on the framework of Winters *et al.* (1995). This begins with the definition of the total potential energy, expressed in dimensionless form as

$$\mathscr{P} \equiv \frac{g}{(\Delta u)^2 \rho_0} \langle \rho z \rangle_V, \tag{2.3}$$

where $\langle \cdot \rangle_V$ denotes a volume average over the computational domain, and g is the acceleration due to gravity. $\mathscr{P}$ can be partitioned into the available potential energy, $\mathscr{P}_A$, and background potential energy, $\mathscr{P}_B$, reservoirs. Here $\mathscr{P}_B$ is defined as

$$\mathscr{P}_B \equiv \frac{g}{(\Delta u)^2 \rho_0} \langle \rho_B z \rangle_V, \tag{2.4}$$

where $\rho_B = \rho_B(z)$ is the background density profile. This profile represents the minimum potential energy state of the density field if fluid elements are rearranged and deformed adiabatically, i.e. without altering their density. Such a profile is a monotonically decreasing function of height. The significance of ρ_B lies in the fact that for a closed domain (as is used here) any changes to this profile are irreversible, and lead to an increased $\mathscr{P}_B$ as time proceeds (Winters *et al.* 1995). These changes are closely linked with the rate of mixing of the density field. It is now possible to define $\mathscr{P}_A$ by

$$\mathscr{P}_A \equiv \mathscr{P} - \mathscr{P}_B. \tag{2.5}$$

This quantity represents the amount of potential energy that is available to be converted back to kinetic energy to drive fluid motions. Unlike the $\mathscr{P}_B$ reservoir, changes in $\mathscr{P}_A$ are reversible and represent 'stirring' processes (Peltier & Caulfield 2003). These relationships can be seen more clearly by looking at the evolution equations for the kinetic and potential energy reservoirs. For a closed domain in

dimensionless form (see Winters *et al.* 1995; Peltier & Caulfield 2003):

$$\frac{\mathrm{d}\mathscr{K}}{\mathrm{d}t} = -J\langle\rho_* w_*\rangle_V - Re^{-1}\langle \boldsymbol{u}_* \cdot \nabla_*^2 \boldsymbol{u}_*\rangle_V = \mathscr{B} + \varepsilon, \tag{2.6}$$

$$\frac{\mathrm{d}\mathscr{P}}{\mathrm{d}t} = J\langle\rho_* w_*\rangle_V + \frac{J}{RePr\,H} = -\mathscr{B} + \Phi, \tag{2.7}$$

where the volume averaged kinetic energy is given by

$$\mathscr{K} = \frac{\langle \boldsymbol{u}\cdot\boldsymbol{u}/2\rangle_V}{(\Delta u)^2} \tag{2.8}$$

and H is the dimensionless domain height. The variables and operators with an asterisk as subscript have been non-dimensionalized by the velocity, length, density and time scales given by Δu, h_0, $\Delta\rho$ and $h_0/\Delta u$, respectively. These scales are used throughout the rest of the paper.

The buoyancy flux, $\mathscr{B}$, represents the reversible transfer of energy between the kinetic and potential energy reservoirs. This can be seen by its presence in (2.7), where it is of opposite sign to (2.6), indicating that transfers exist between both reservoirs. The last term in (2.6), ε, gives the average loss of kinetic energy owing to viscous dissipation. This constitutes an irreversible transfer from $\mathscr{K}$ to the internal energy reservoir of the fluid. Since ε acts most effectively on the small scales of velocity variation, it can be used as an indicator for the level of turbulence present in the flow. The last term in (2.7), Φ, represents the irreversible rate of increase of $\mathscr{P}$ owing to the molecular diffusion of the initial density profile. In this representation, it has been assumed that $\bar{\rho}_{bottom} - \bar{\rho}_{top} = \Delta\rho$, where $\bar{\rho}_{bottom}$ and $\bar{\rho}_{top}$ denote the average density on the bottom and top vertical domain boundaries. This assumption holds for sufficiently large domain heights such that the average density at the vertical domain boundaries remains constant, and the difference is always $\Delta\rho$. This term plays only a minor role in the dynamics of high-Re and high-Pr mixing events. However, since the present study is constrained to relatively low Re and Pr, the energy transfer by Φ represents a non-negligible component of the dynamics, and serves to quantify the rate of increase in $\mathscr{P}$ that occurs in the absence of fluid motion.

In order to quantify the rate of fluid mixing, similar equations are written for $\mathscr{P}_A$ and $\mathscr{P}_B$ as follows:

$$\frac{\mathrm{d}\mathscr{P}_A}{\mathrm{d}t} = -\mathscr{B} - \mathscr{M}, \tag{2.9}$$

$$\frac{\mathrm{d}\mathscr{P}_B}{\mathrm{d}t} = \mathscr{M} + \Phi. \tag{2.10}$$

Here, $\mathscr{M}$ represents the instantaneous mixing rate, defined as the rate of increase in $\mathscr{P}_B$ due solely to fluid motions (Peltier & Caulfield 2003).

Since changes in $\mathscr{P}_B$ can be computed easily by a simple sorting of the density field, this quantification of the mixing rate lends itself well to the numerical simulations performed here. The interaction between various energy reservoirs described by evolution equations (2.6)–(2.10) are shown schematically in figure 4. The partition of $\mathscr{P}$ into $\mathscr{P}_A$ and $\mathscr{P}_B$ allows for the distinction between stirring and mixing processes. Stirring processes are associated with reversible energy transfers between $\mathscr{P}_A$ and $\mathscr{K}$, and mixing processes are due exclusively to the irreversible transfer of energy to $\mathscr{P}_B$ from $\mathscr{P}_A$.

It is also instructive to partition $\mathscr{K}$ into components that can be associated with the kinetic energy of motions related to the mean flow, the two-dimensional

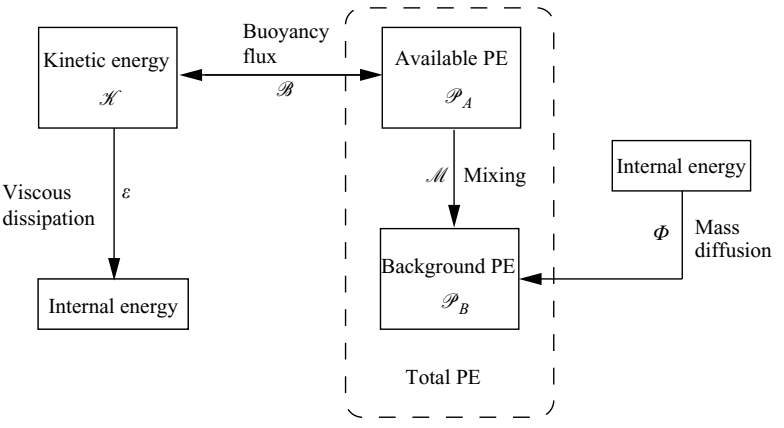

FIGURE 4. Illustration of the relationships between the various energy reservoirs and the transfers between them. Bidirectional arrows indicate reversible transfers whereas unidirectional arrows represent irreversible transfers (after Winters *et al.* 1995).

primary instability, and the three-dimensional secondary instabilities and subsequent turbulence. Following Caulfield & Peltier (2000), this is done as follows:

$$\bar{\mathscr{K}} = \frac{1}{(\Delta u)^2}\langle(\bar{\boldsymbol{u}}\cdot\bar{\boldsymbol{u}})/2\rangle_z, \tag{2.11a}$$

$$\mathscr{K}_{2d} = \frac{1}{(\Delta u)^2}\langle(\boldsymbol{u}_{2d}\cdot\boldsymbol{u}_{2d})/2\rangle_{xz}, \tag{2.11b}$$

$$\mathscr{K}_{3d} = \frac{1}{(\Delta u)^2}\langle(\boldsymbol{u}_{3d}\cdot\boldsymbol{u}_{3d})/2\rangle_{xyz}, \tag{2.11c}$$

where

$$\bar{\boldsymbol{u}}(z,t) = \langle\boldsymbol{u}\rangle_{xy}, \tag{2.12a}$$

$$\boldsymbol{u}_{2d}(x,z,t) = \langle\boldsymbol{u}-\bar{\boldsymbol{u}}\rangle_y, \tag{2.12b}$$

$$\boldsymbol{u}_{3d}(x,y,z,t) = \boldsymbol{u}-\bar{\boldsymbol{u}}-\boldsymbol{u}_{2d}, \tag{2.12c}$$

and $\langle\cdot\rangle_i$ represents an average in the component direction i. From these definitions it follows that

$$\mathscr{K} = \bar{\mathscr{K}} + \mathscr{K}_{2d} + \mathscr{K}_{3d}.$$

It is important to note that the exchange between these reservoirs is reversible, implying that energy may be transferred directly from $\mathscr{P}_A$ via $\mathscr{B}$ to any of the kinetic energy reservoirs.

2.4. *Mixing efficiency*

In the study of stratified flows, the efficiency of a mixing event has been defined as the ratio of the increase in potential energy of the system to the work done by the kinetic energy of the driving mechanism (Caulfield & Peltier 2000). In this case, kinetic energy is extracted from the shear layer, and work is done by the instability on the fluid through mixing of the density field, and in losses due to viscous dissipation. With this in mind, a suitable measure of the mixing efficiency can be arrived at by inspection of the energy evolution equations (2.6)–(2.10). First, note that if a reservoir is defined that consists of both $\mathscr{K}$ and $\mathscr{P}_A$, then the reversible transfer associated with $\mathscr{B}$ is eliminated and all transfers between reservoirs are irreversible. It can be

seen that the energy consumed by the mixing event can be used for two different processes: to be lost to the internal energy of the fluid by viscous dissipation, or to be used to mix the density field and supply background potential energy. So by defining the instantaneous mixing efficiency, $\mathscr{E}_i$, as

$$\mathscr{E}_i \equiv \frac{\mathscr{M}}{\mathscr{M} + \varepsilon}, \tag{2.13}$$

we are taking the ratio of the rate at which the mixing event is supplying potential energy, to the total rate at which energy is being lost in the process. This definition is equivalent to that discussed in Caulfield & Peltier (2000) and Peltier & Caulfield (2003), and has the property $0 \leqslant \mathscr{E}_i < 1$.

Also of interest is the flux coefficient $\Gamma_i = \mathscr{M}/\varepsilon'$. Here the viscous dissipation has been split into mean and fluctuating components $\varepsilon = \varepsilon' + \bar{\varepsilon}$, where the dissipation of the mean flow is given in dimensionless form by

$$\bar{\varepsilon} = -Re^{-1} \left\langle \left(\frac{\mathrm{d}\bar{u}}{\mathrm{d}z} \right)^2 \right\rangle_V . \tag{2.14}$$

The flux coefficient is often used in approximating turbulent mixing based on dissipation measurements in field studies (e.g. Smyth *et al.* 2001) and is the ratio of the rate of increase in potential energy to the rate of kinetic energy loss of the disturbance.

Of course $\mathscr{E}_i$ and Γ_i alone are not sufficient to describe the mixing behaviour in a particular flow – the magnitude of the energy transfers are also important. For example, if both $\mathscr{M}$ and ε are small then $\mathscr{E}_i$ may be close to unity, indicating highly efficient mixing, yet the transfers themselves may not represent a significant mixing process.

It is also useful to define a cumulative mixing efficiency and flux coefficient as

$$\mathscr{E}_c \equiv \int_T \mathscr{M}\, \mathrm{d}t \Bigg/ \left(\int_T \mathscr{M}\, \mathrm{d}t + \int_T \varepsilon\, \mathrm{d}t \right), \tag{2.15}$$

and

$$\Gamma_c \equiv \int_T \mathscr{M}\, \mathrm{d}t \Bigg/ \int_T \varepsilon'\, \mathrm{d}t, \tag{2.16}$$

where T denotes some duration of interest (Peltier & Caulfield 2003). If T is taken as the total duration of a mixing event, then $\mathscr{E}_c$ gives the total proportion of energy that is used to perform mixing to the total amount of energy expended in the process. This gives an indication of the mixing efficiency of the entire event, rather than an instantaneous value.

3. Numerical solution method

3.1. *Description of numerical model*

The numerical simulations performed in this study were carried out using a three-dimensional spectral model designed for the study of stratified flows (see Winters, MacKinnon & Mills 2004 for a full discussion). It is used here to solve the incompressible equations of motion for a Boussinesq fluid in the absence of external forces and rotational effects described by

$$\frac{\mathrm{D}\boldsymbol{u}}{\mathrm{D}t} = -\frac{1}{\rho_0}\nabla p - \frac{\rho}{\rho_0} g\hat{\boldsymbol{k}} + \nu\nabla^2\boldsymbol{u} \tag{3.1}$$

and

$$\nabla \cdot \boldsymbol{u} = 0. \tag{3.2}$$

Here $\mathrm{D}/\mathrm{D}t = \partial/\partial t + \boldsymbol{u}\cdot\nabla$ denotes a material derivative and $\hat{\boldsymbol{k}}$ is the unit vector in the vertical direction (positive upwards). The pressure field is given by p, and the density field by ρ. Since the density field is governed by an active scalar it evolves subject to the advection–diffusion equation

$$\frac{\mathrm{D}\rho}{\mathrm{D}t} = \kappa\nabla^2\rho. \tag{3.3}$$

For the purposes of this study any nonlinearities in the equation of state are neglected.

Since the viscous and diffusive terms from (3.1) and (3.3) are purely molecular this numerical solution method fits into the direct numerical simulations (DNS) category. Owing to the present limitations involving computational resources, DNS is constrained to study flows with relatively small domain sizes, and lower values of Re and Pr than would often occur in nature. In the DNS of a homogenous fluid, the difficulty of simulating high-Re flows lies in the large range of length-scale variability, where the largest scales are generally given by the domain size, and the smallest scales are $O(L_K)$ (Moin & Mahesh 1998). Here, $L_K = (\nu^3/\epsilon)^{1/4}$ is the Kolmogorov length scale, where ϵ is the rate of viscous dissipation. This represents the scale at which velocity gradients are diffusively smoothed by viscosity. However, in a stratified flow where $Pr > 1$, as is the case here, the smallest scales are determined by the Batchelor length $L_B = L_K/Pr^{1/2}$ (Batchelor 1959). This expresses the fact that the smallest scales are now determined by scalar gradients smoothed by molecular diffusion – a relatively slower process. High Pr fluids are therefore able to generate significantly smaller scales than realized in otherwise homogenous flows.

This limitation has been partially alleviated by a modification of the Winters *et al.* (2004) model to aid in the simulation of higher Pr fluids. The modification includes an additional active scalar field that is resolved on a grid twice as fine as the velocity and pressure grids. Originally designed for the study of differential diffusion, i.e. the mixing of two scalar fields with different Pr (see Smyth, Nash & Moum 2005), it is used here for a single scalar at moderate Pr.

3.2. *Initial and boundary conditions*

In order to reduce the number of time steps required for the initial growth of the primary instability, a perturbation is applied to the initial velocity and density fields. The perturbation varies only in the streamwise direction (as the primary instability is two-dimensional, confirmed by Haigh & Lawrence 1999; Smyth & Peltier 1990) and is determined from the solution of the Taylor–Goldstein equation incorporating the effects of viscosity and mass diffusion.

Solution of the Taylor–Goldstein equation predicts the structure of the resulting instability, given by the eigenfunctions, as well as the growth rate and phase speed for a disturbance of a given wavenumber, as found in the eigenvalues. Since it is generally found that the wavenumber of the fastest growing mode dominates the nonlinear development of the flow (Lawrence *et al.* 1991), the perturbation is applied at the wavenumber of maximum growth rate. Solution of the Taylor–Goldstein equations is based on linear theory and assumes that the perturbations have infinitesimally small amplitude. For this reason, the perturbation must be small enough to ensure it spends some time in the linear regime and does not adversely affect the nonlinear growth of the instability. A maximum displacement amplitude of $0.1h_0$ was found to be sufficient for these purposes.

	Simulation number						
	1	2	3	4	5	6	7
a	0	0	0.25	0.50	1.0	1.5	2.0
R	1	3	3	3	3	3	3
N_x	128	192	128	128	128	128	128
N_y	96	96	96	96	96	96	96
N_z	192	192	192	192	192	192	192
L_x/h_0	6.98	8.97	6.16	5.71	5.71	6.04	6.28
σ	0.081	0.023	0.090	0.131	0.163	0.172	0.176

TABLE 1. Summary of numerical simulations performed. Here, $\{N_x, N_y, N_z\}$ refer to the number of points used in each dimension of the coarse grid. The finer mesh has double the resolution of the coarse grid. Dimensionless growth rates obtained from linear theory are given by σ for each simulation.

In addition to the perturbation described above, a random perturbation is applied to the velocity field to stimulate the growth of three-dimensional secondary instabilities. The amplitude of the perturbation is evenly distributed in the range $\pm 0.005\Delta u$, and is centred on the density interface (see SW03 for details).

The computational domain consists of lengths in each of the streamwise, spanwise and vertical directions denoted by $\{L_x, L_y, L_z\}$, respectively. The boundary conditions are periodic in both the streamwise and spanwise directions so that L_x is given by the fastest growing wavelength determined by the linear stability analysis. The streamwise extent, therefore, varies for each simulation. In order to accommodate a number of wavelengths of the resulting secondary instabilities, all simulations have $L_y = 4.5h_0$. This estimate is based on the observations of secondary instabilities from KH and Holmboe simulations in Caulfield & Peltier (2000) and SW03. The no-flux free-slip boundary conditions are employed in the vertical directions requiring the vertical velocity and vertical fluxes to vanish, i.e.

$$w|_{z=0,L_z} = \left.\frac{\partial u}{\partial z}\right|_{z=0,L_z} = \left.\frac{\partial v}{\partial z}\right|_{z=0,L_z} = 0, \qquad \left.\frac{\partial \rho}{\partial z}\right|_{z=0,L_z} = 0. \tag{3.4}$$

A value of $L_z = 9h_0$ was chosen such that the vertical boundaries are large enough to have a negligible influence on the development of the instability. A summary of the simulations discussed in this study is shown in table 1.

4. Results

4.1. *The symmetric case: KH and Holmboe instabilities*

Simulation results are examined first in the symmetric case ($a = 0$), where KH and Holmboe instabilities are found to develop. This gives a basis for comparison in the asymmetric cases ($a \neq 0$), and helps illustrate the effects that asymmetry has on the flow.

4.1.1. *Kelvin–Helmholtz case*

The evolution of the KH instability can be seen in the two-dimensional (x, z)-slices of the density field shown in figure 5. These slices are taken at the centre of the spanwise domain ($y = L_y/2$) and are similar to visualizations of the density field encountered in laboratory investigations where light sheets are used to illuminate the

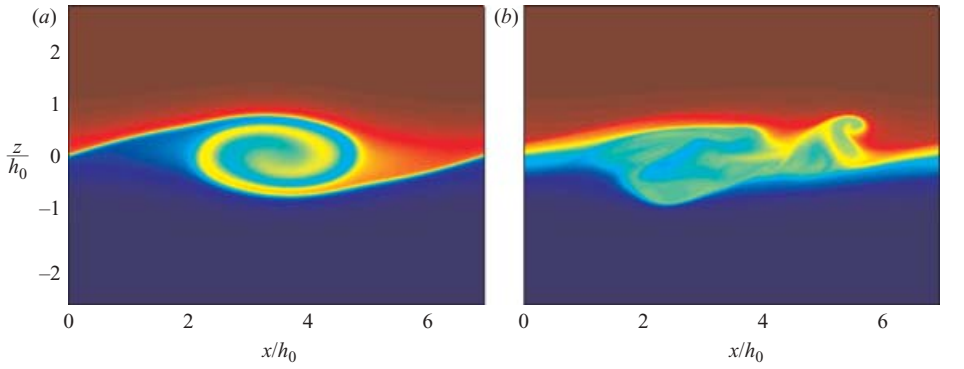

FIGURE 5. Plots of the density field in the KH simulation showing its initial development (*a*), and a time of turbulent motion (*b*). Slices of the (x, z)-plane are taken at $y = L_y/2$ with non-dimensional times (*a*) $t = 45$, (*b*) $t = 104$.

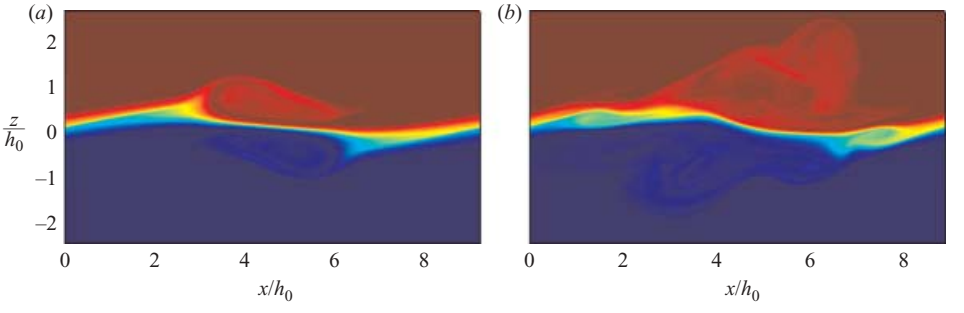

FIGURE 7. Plots of the density field in the Holmboe simulation showing its initial development (*a*), and a time of turbulent motion (*b*). Slices of the (x, z)-plane are taken at $y = L_y/2$ with non-dimensional times (*a*) $t = 89$, (*b*) $t = 200$.

flow (e.g. Lawrence *et al.* 1991; Schowalter, Van Atta & Lasheras 1994; Hogg & Ivey 2003).

The initial development of instability is characterized by the formation of a locally unstable billow region in which a large-scale overturning of the central isopycnal is accomplished. This process of primary growth is essentially two-dimensional and sees the entrainment of interfacial fluid into the billow core. Once the overturn is initiated, three-dimensional secondary structures grow mainly within the statically unstable regions of the billow (this aspect of KH instabilities has been examined in detail in Klaassen & Peltier 1991). As the flow within the billow becomes increasingly complex, the transition to turbulence is observed. With the transition comes a breakdown of the primary billow and a lateral spreading of the mixed core of fluid. Turbulence decay and restratification are then observed. It should be noted that the term 'turbulence' is being used loosely in the above description and throughout the rest of the paper to indicate a region of complex or chaotic flow structure, and the low *Re* used may preclude this flow from fitting descriptions of turbulent mixing in other studies (e.g. Dimotakis 2000, 2005).

The above description can be made more quantitative by examining the energy exchange as outlined in § 2.3. Figure 6 shows the evolution of the potential energy reservoirs, the irreversible transfers $\mathscr{M}$, ε' and $\bar{\varepsilon}$, and the flux coefficient Γ_i and mixing

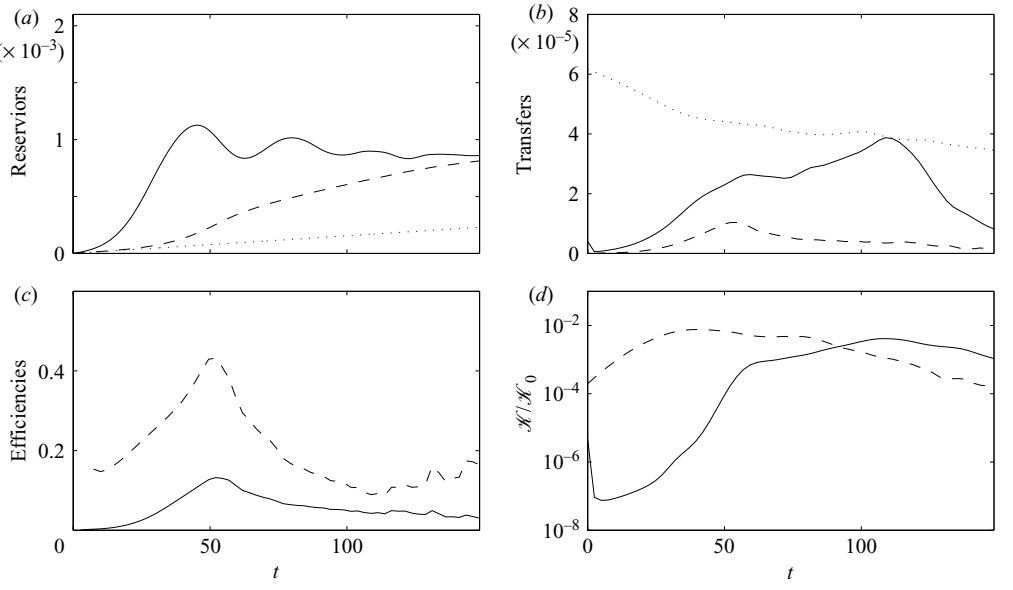

FIGURE 6. Energy reservoirs and transfers for the KH simulation. The plot in (*a*) includes the potential energy reservoirs $\mathscr{P}$ (solid line), $\mathscr{P}_B$ (dashed line), and $\int \Phi \, \mathrm{d}t$ (dotted line). In (*b*) the irreversible transfers ε' (solid line), $\bar{\varepsilon}$ (dotted line) and $\mathscr{M}$ (dashed line) are shown along with $\mathscr{E}_i$ (solid line) and Γ_i (dashed line) in (*c*). The $\mathscr{K}_{2d}$ (dashed line) and $\mathscr{K}_{3d}$ (solid line) reservoirs are plotted in (*d*) where they are expressed as a fraction of the initial kinetic energy $\mathscr{K}_0 = \mathscr{K}(0)$.

efficiency $\mathscr{E}_i$ for the KH instability with all times non-dimensionalized by $h_0/\Delta u$. Figure 6(*a*) shows a relatively rapid growth in $\mathscr{P}_A$ (obtained from the difference between $\mathscr{P}$ and $\mathscr{P}_B$) owing to the roll-up of the primary billow. At $t \approx 45$, the flow has reached its state of maximum potential energy (and maximum $\mathscr{P}_A$) when the billow has saturated. Shortly after this time, the billow core begins to collapse owing to the growth of three-dimensional secondary instabilities which appear to be associated with the locally unstable regions around the billow core. Thus far, the rate of mixing has steadily increased until its peak at $t \approx 50$. At this time, the secondary instabilities have evolved into coherent structures within the billow core. These structures resemble those observed in the stratified mixing-layer experiments of Schowalter *et al.* (1994). However, the flow within the billow (or elsewhere) cannot be called turbulent; but, it is on the verge of turbulent collapse. As can be seen in figure 5, the greater degree of mixing within the core region has produced a 'pocket' of intermediate density fluid that is vertically centred between the two relatively undisturbed layers. Through a combination of both buoyancy forces and the background shear, this pocket spreads laterally throughout the centre of the domain where the density profile assumes a statically stable configuration as the flow relaminarizes.

By inspection of figure 6(*b*), it can be seen that the highest levels of viscous dissipation occur well after the highest levels of mixing, and can be identified with the lateral spreading and shearing of the mixed billow core. In this stage of the flow, the surplus of $\mathscr{P}_A$ gained initially by the billow roll-up has largely been consumed. With no other stirring mechanism present for the formation of $\mathscr{P}_A$, the small-scale turbulent motions have little effect on mixing. This general trend can be seen in figure 6(*c*), where both $\mathscr{E}_i$ and Γ_i peak in the early stages of 'preturbulent mixing'

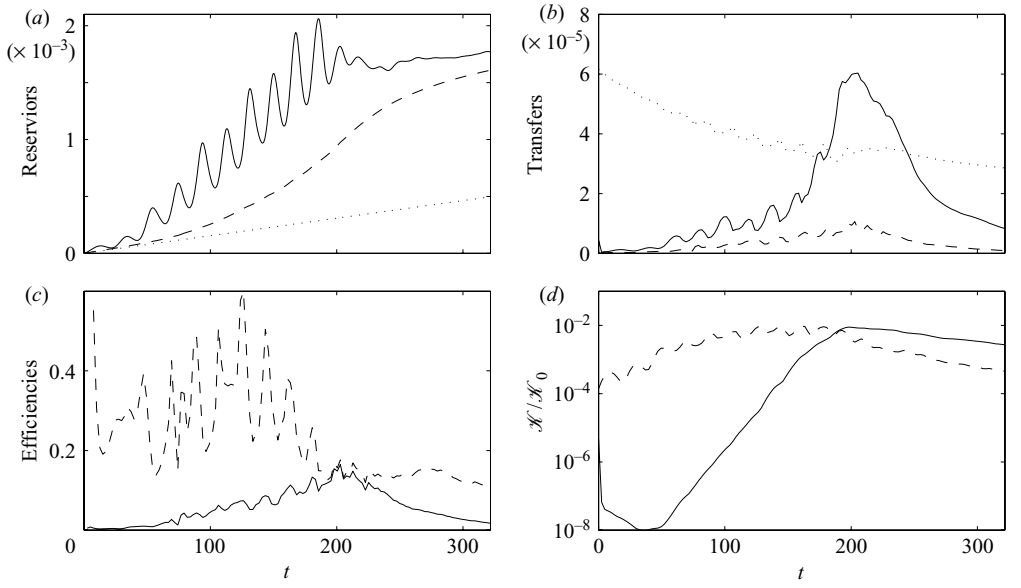

FIGURE 8. Energy reservoirs and transfers for the Holmboe simulation. Details as in figure 6.

(to use the terminology of SW03), whereas the later stages are marked by a much lower efficiency corresponding to the collapse of the core region. Attention should be given to the low levels of ε' attained in this KH simulation. Previous studies by Caulfield & Peltier (2000) and Staquet (2000) show significantly greater levels of ε'. This is expected to be a feature of the low Re on the KH billow at this particular J.

Through examination of figure 6(d), the initial stage of primarily two-dimensional growth can be seen in the exponential growth of the $\mathscr{K}_{2d}$ reservoir. A more rapid growth of $\mathscr{K}_{3d}$ follows once significant statically unstable density regions have formed at $t \approx 25$. This rapid and relatively constant growth rate of $\mathscr{K}_{3d}$ continues until $t \approx 60$ – shortly after the time of greatest mixing. The $\mathscr{K}_{3d}$ reservoir then slowly peaks at the time when ε' is largest and gradually drops off as relaminarization occurs.

4.1.2. *Symmetric Holmboe case*

As the scale ratio R, is increased, the stratification is compressed to a layer thinner than the shear thickness. While J remains unchanged, the density gradient is locally sharpened in the centre of the domain. This results in the formation of Holmboe's instability as seen in figure 7, p. XXX. The growth of Holmboe's instability is considerably slower than that of the KH, as is expected from its smaller linear growth rate (see table 1 for the linear growth rate σ, for each simulation).

Before the onset of turbulent motions, the energy characteristics shown in figure 8 can be seen to be marked by a pronounced oscillation. This is due to a standing wavelike motion that develops during the growth of the instability. This motion is caused by the interaction of the upper and lower modes to produce a reversible transfer of energy between the $\mathscr{K}$ and $\mathscr{P}$ reservoirs by the buoyancy flux $\mathscr{B}$. The result is an oscillation of the primary density interface that is in phase with the passage of the upper and lower modes. Irreversible transfers are also taking place through ε' and $\mathscr{M}$ that exhibit the same oscillation (figure 8b). As was shown in SW03, both the net amount of mixing (given by $\int \mathscr{M}\, \mathrm{d}t$) and ε' attain higher levels in the Holmboe instability than the KH. Once the turbulent transition is reached at

$t \approx 200$, the waves breakdown and release the last of the $\mathscr{P}_A$ and $\mathscr{K}$ that was attained during the preturbulent growth phase. This aspect of symmetric Holmboe instabilities is discussed in greater detail in Smyth, Carpenter & Lawrence (2007).

Secondary instability (indicated by $\mathscr{K}_{3d}$) is not evident until $t \approx 60$. Once the growth of $\mathscr{K}_{3d}$ begins, it is at a lower rate than the KH simulation and is not strongly influenced by the standing-wave motion. Secondary motions are described in detail by Smyth (2007), and consist of horizontal shear production in the lee of the wave crests, as well as sloping convection in the crests. At no point in the simulation are large-scale overturns of the central isopycnal present. The mixing accomplished by the Holmboe instability is due to other processes that leave the density interface relatively intact. These will be discussed in the following in the context of AH instabilities as well.

4.2. *The asymmetric case: AH instabilities and the effects of asymmetry*

A series of simulations is now presented in which the asymmetry factor, a, is gradually increased while leaving all other parameters constant (with the exception of L_x as discussed in § 3.2). Note that in these simulations $R = 3$, and the resulting instabilities appear more closely associated with the Holmboe modes observed in the symmetric case. Linear stability analysis of the asymmetric configurations shows the presence of two modes of instability: a dominant mode with a larger growth rate that forms on the side of the density interface with a greater fraction of initial shear-layer vorticity, and a weaker mode with small growth rate in the opposite layer (Lawrence *et al.* 1991; Haigh 1995). However, for all simulations performed in this study, the value of J chosen results in the stabilization of the weaker mode according to linear theory. As can be seen in the evolution of the density fields in the following simulations, only the dominant AH mode develops initially (owing in part to the initial perturbation and streamwise periodic boundary conditions) and grows more rapidly than both the KH and Holmboe instabilities, as is expected from its larger linear growth rate (cf. table 1).

4.2.1. $a = 0.25$ *case*

The energy characteristics for the $a = 0.25$ asymmetry are shown in figure 9. Initially, the potential energy of the $a = 0.25$ AH instability bears resemblance to the KH case, where there is a rapid growth of $\mathscr{P}_A$ owing to the formation of a billow structure. This billow is qualitatively different from standard KH billows in that it never accomplishes a complete overturning of the central isopycnal; leaving the density interface intact, it draws fluid of intermediate density from the upper portions of the interface (figure 10). The billow structure thins soon after its initial development to resemble more closely a Holmboe mode, where a cusp-like wave forms that is continually entraining a wisp of fluid into the leading vortex, located in the dominant upper layer. This entrainment process supplies $\mathscr{P}_A$ which is then mixed within the primary vortex at a relatively steady rate (figure 9*b*). Mixing continues in this manner for a substantial period of time ($t \approx 45 - 110$) during which secondary instabilities grow within the primary vortex.

This preturbulent period shows a developing three-dimensional structure that remains coherent. As in the KH simulation, this coherent mixing stage is marked by the highest levels of $\mathscr{E}_i$ and Γ_i. The secondary instabilities also appear to be associated with the statically unstable regions created in the primary vortex, similar to the KH case. Figure 11 shows the development of this three-dimensional motion in the (y, z)-plane taken from the trailing edge of the primary vortex slightly downstream

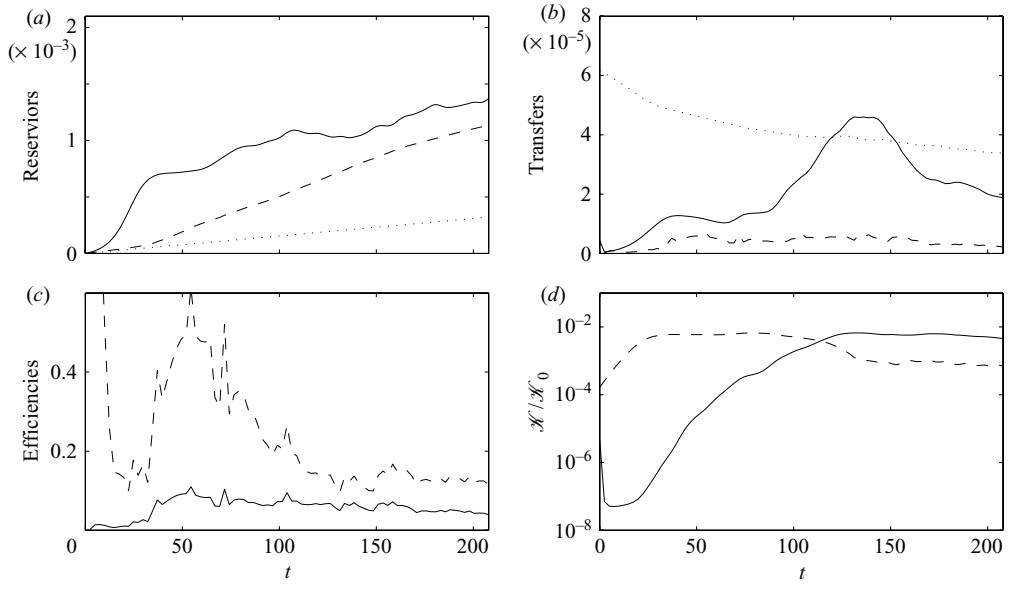

FIGURE 9. Energy reservoirs and transfers for the $a = 0.25$ simulation. Details as in figure 6.

of the cusp in the later stages of the preturbulent period ($t = 89$). Density structure similar to this was observed in the mixing-layer experiments of Schowalter *et al.* (1994) where the locally unstable stratification led to the amplification of streamwise vortices through the baroclinic generation of vorticity (see their figure 26*a* in particular).

The breakdown of the primary vortex to incoherent three-dimensional motions is reflected in the rise of ε' with a maximum at $t \approx 140$, after the majority of the mixing has occurred. However, the rate of mixing remains relatively constant, and begins to trail off only after the turbulence begins to decay and the upper layer relaminarizes. This indicates that the turbulent motions are mixing previously entrained – but not completely mixed – fluid in the dominant layer.

It should be noted that towards the end of the simulation the weaker mode is observed to develop in the lower layer. The development of this mode is perhaps not surprising considering that the density gradient of the weaker layer remains sharp while an appreciable amount of shear-layer vorticity remains. However, it is possible that the growth of the weaker mode has been compromised somewhat owing to the periodic streamwise boundary condition. This boundary condition forces the mode to develop at only those wavenumbers that are harmonics of the streamwise domain length L_x. In general, the results of linear stability analysis show that the weaker mode has maximum growth rates at higher wavenumbers than the dominant mode (Haigh 1995). The simulation was not carried out for long enough to quantify the behaviour of the weaker mode.

The growth of both primary and secondary instabilities can be seen in the $\mathscr{K}_{2d}$ and $\mathscr{K}_{3d}$ curves in figure 9(*d*), respectively. Here the kinetic energy associated with the primary instability, $\mathscr{K}_{2d}$, grows at a near constant exponential rate until $t \approx 25$, corresponding to the time at which the initial billow structure begins to thin. This time marks the beginning of secondary growth given by $\mathscr{K}_{3d}$. The initial growth rate of secondary instabilities can be inferred from the slope of this curve, and is seen to be larger than that of the primary instability. This is in agreement with the results for symmetric stratified shear layers in SW03 and Caulfield & Peltier (2000). As the $\mathscr{K}_{3d}$

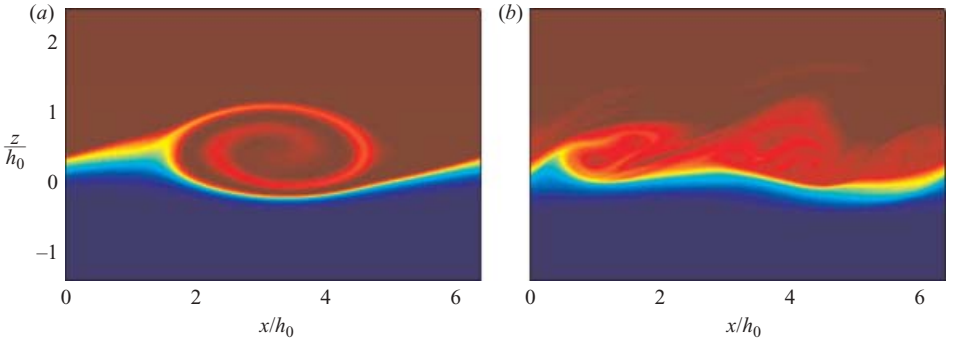

FIGURE 10. Plots of the density field in the $a = 0.25$ simulation showing a time of initial development (a), and a time of turbulent motion (b). Slices of the (x, z)-plane are taken at $y = L_y/2$ with non-dimensional times (a) $t = 45$, (b) $t = 141$.

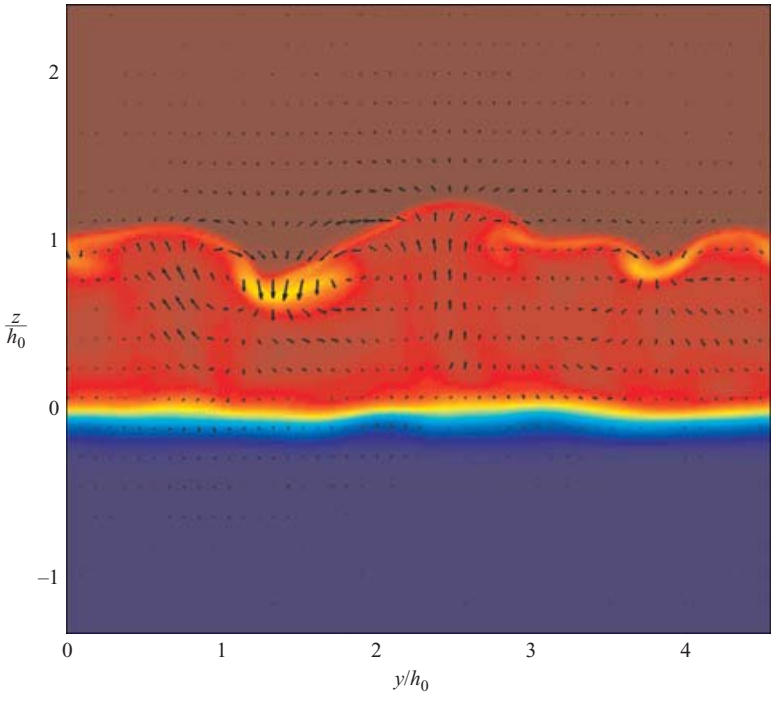

FIGURE 11. Cross-section in the (y, z)-plane of the density field with $\boldsymbol{u}_{3d}$ vectors overlaid for the $a = 0.25$ simulation. The streamwise location is taken within the primary vortex for $x = 4h_0$ at dimensionless $t = 89$.

reservoir reaches appreciable levels, $\mathscr{K}_{2d}$ begins to decay as transition occurs. By the end of the simulation the signature of the weaker mode can be seen in the levelling off of the $\mathscr{K}_{2d}$ curve with a pronounced oscillation as it interacts with residual motions on the density interface.

4.2.2. $a = 0.50$ *case*

As the asymmetry is increased to $a = 0.50$, both similarities and departures from the $a = 0.25$ case can be seen. In figure 12, a sharp rise in $\mathscr{P}_A$ can be seen as a

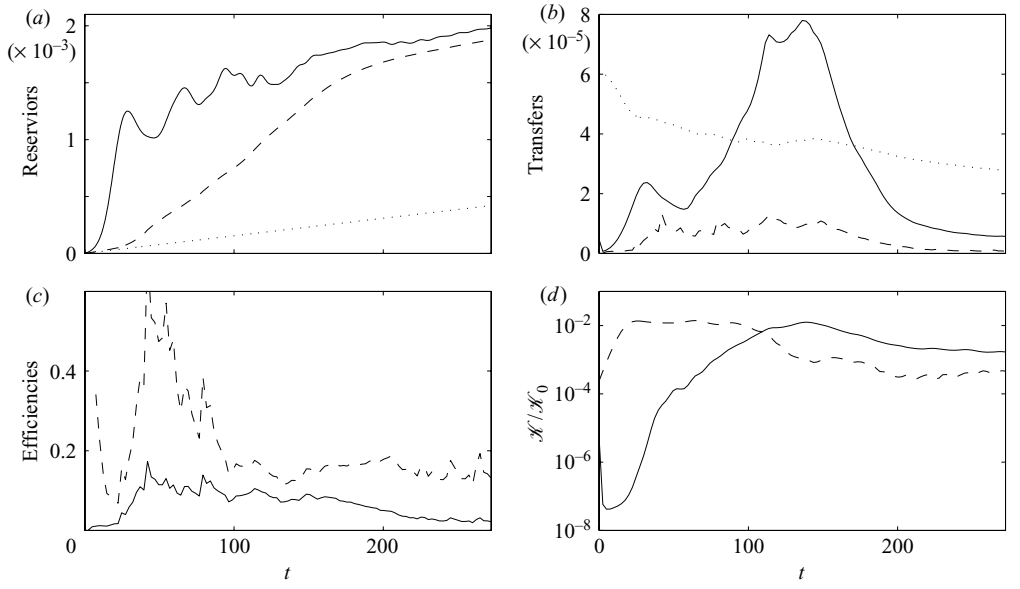

FIGURE 12. Energy reservoirs and transfers for the $a = 0.50$ simulation. Details as in figure 6.

billow structure develops. The quicker formation of the intial instability is consistent with the high growth rate predicted by linear theory. By examining the density field in figure 13(a), it can be seen that the billow grows to a larger diameter than in the $a = 0.25$ case. This is not surprising since the dominant layer has a greater fraction of the initial shear-layer vorticity available. The rapid development of the AH instability leads to a considerably larger $\mathscr{P}_A$ increase in this case, and appears to have overshot the amount of dense fluid that it can entrain in the primary vortex. This is suggested by the subsequent thinning of the initial billow to produce the cusp-like wave structure shown in figure 13(a). Remnants of the energetic initial growth can be seen in the portion of dense fluid that has been entrained into the primary vortex (at the bottom right of the vortex in figure 13a). In this respect, the initial development of the AH instability resembles a transient ejection event rather than the steady roll-up of a KH-like billow. This description of the initial development becomes clearer as the asymmetry is increased further, discussed in following paragraphs.

Following initial development, the flow enters a preturbulent period in which the majority of the mixing is accomplished. Just as in the $a = 0.25$ case, this period sees the growth of secondary instabilities leading to the turbulent transition indicated by elevated levels of ε' starting at $t \approx 100$. Throughout both the preturbulent and turbulent phases the mixing stays relatively constant with small changes present in the turbulent phase and in periods associated with ejection events. Again, the preturbulent phase is found to be the most efficient, with a gradual decline following the development of a more complex flow structure. During the preturbulent phase, high levels of mixing are maintained by the entrainment of fluid from the upper portions of the density interface by the primary vortex. Since the entrained fluid is of only intermediate density, there appears to be no saturation of the primary vortex as is found in KH instabilities. This entrainment and mixing of the interface leads to sharper scalar gradients and higher mass fluxes.

The amplification of streamwise vorticity by locally unstable regions still appears to be a prominant cause of three-dimensional motions. However, a more complex

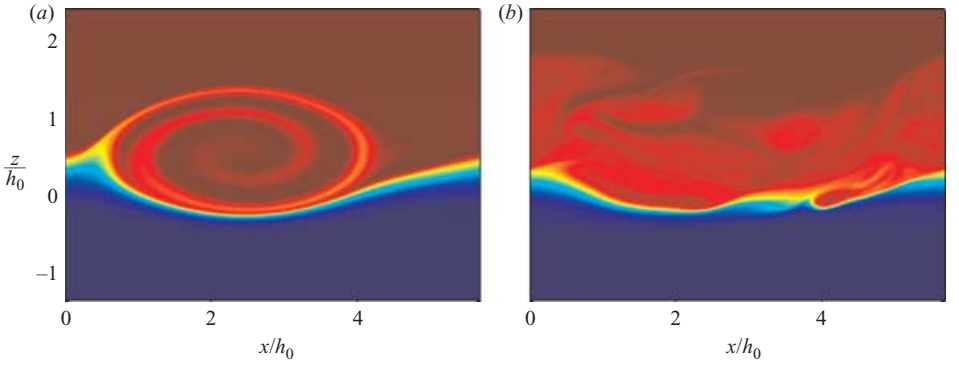

FIGURE 13. Plots of the density field in the $a = 0.50$ simulation showing a time of initial development (a), and a time of turbulent motion (b). Slices of the (x, z)-plane are taken at $y = L_y/2$ with non-dimensional times (a) $t = 45$, (b) $t = 141$.

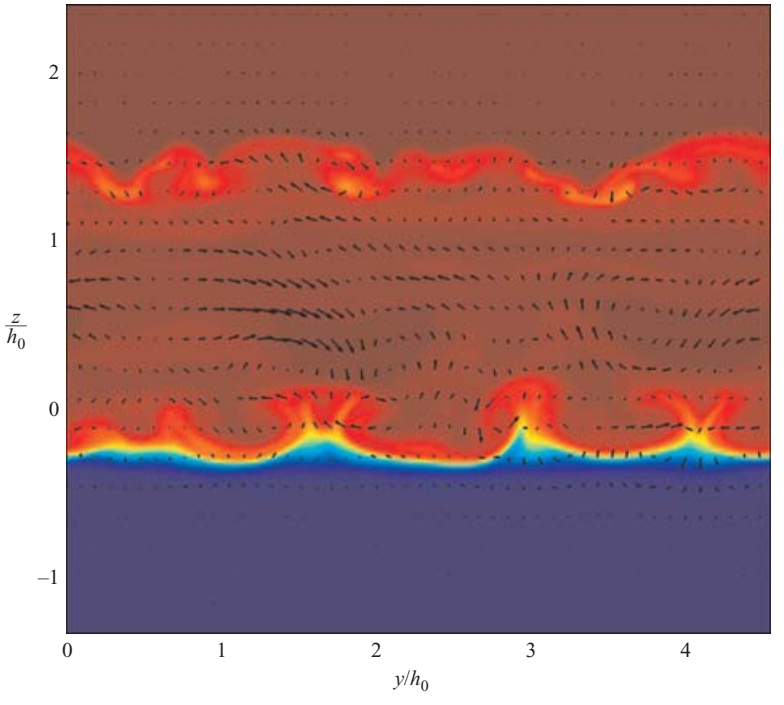

FIGURE 14. Cross-section in the (y, z)-plane of the density field with $\boldsymbol{u}_{3d}$ vectors overlain for the $a = 0.50$ simulation. The streamwise location is taken within the primary vortex for $x = 4h$ at $t = 89$.

interaction between the streamwise vortices and the density interface is observed for $a = 0.50$. This consists of a three-dimensional entrainment of fluid from the density interface within the primary vortex (figure 14). By examining the growth of $\mathscr{K}_{3d}$ in figure 12(d) it can be seen that these two processes are intimately linked. The evolution of $\mathscr{K}_{2d}$ and $\mathscr{K}_{3d}$ appear qualitatively similar to the $a = 0.25$ simulation. However, there is a notable change in the growth rate of $\mathscr{K}_{3d}$ beginning at $t \approx 45$ corresponding to the sinking of the initial ejection to the level of the density interface.

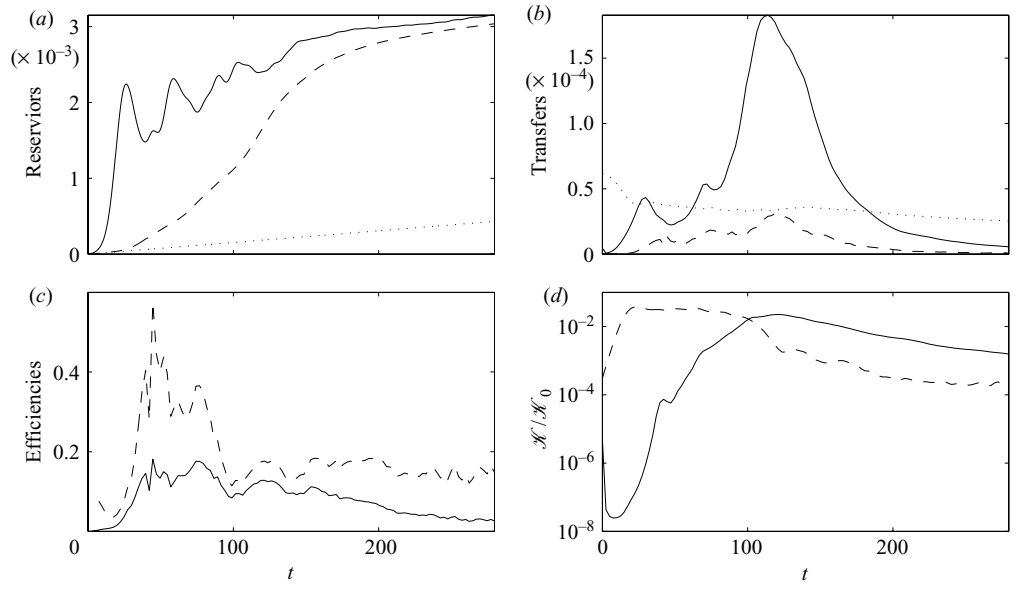

FIGURE 15. Energy reservoirs and transfers for the $a = 1.0$ simulation. Details as in figure 6.

The approach of the dense ejection to the underlying interface can be noted in figure 13(a) in the right-hand side and bottom of the primary vortex, where there is a slight accumulation of dense fluid. In this position, the development of three-dimensional motions appears to be suppressed by the stable stratification of the density interface. This can be seen in the brief period of decreasing $\mathscr{K}_{3d}$ taking place for $\approx 2h_0/\Delta u$ time scales at $t \approx 50$. This relationship between the growth of three-dimensional motions and ejection events can be seen more clearly as the asymmetry is increased and is discussed in greater detail in the following section with respect to the $a = 1$ case.

4.2.3. $a = 1.0$ *case*

A further increase in the asymmetry to $a = 1.0$ results in the energy characteristics shown in figure 15. Again, the higher growth rate and greater fraction of initial shear-layer vorticity available leads to the rapid formation of $\mathscr{P}_A$. This initial spike drops considerably owing to the immediate break-off and vertical settling of the dense ejection of fluid at the bottom of the primary vortex. This process is demonstrated in figure 16(a–c), where slices of the density field are shown with contours of a spanwise average of $\mathscr{K}_{3d}$. The times of these plots are taken before, during, and after the suppressed growth of $\mathscr{K}_{3d}$ shown in figure 15(d) occurring at $t \approx 45$. It can be seen that the highest levels of $\mathscr{K}_{3d}$ are concentrated in the dense ejection. In figure 16(b), the instability is in a phase where the energy of the secondary structures is in a state of decay. In this state, the dense ejection has come into close contact with the underlying density interface, and is the highest concentration of $\mathscr{K}_{3d}$. This indicates that the stability of the interface is acting to suppress the growth of secondary structures in the ejection.

The view proposed in the $a = 0.5$ case (§4.2.2), that the initial development of the instability is best thought of as an ejection event, is now clear. It can be characterized by a rise and fall in $\mathscr{P}_A$ followed by slightly higher values of ε' and $\mathscr{M}$. This same signature can also be seen at a later time of $t \approx 55 - 75$ where a second ejection is

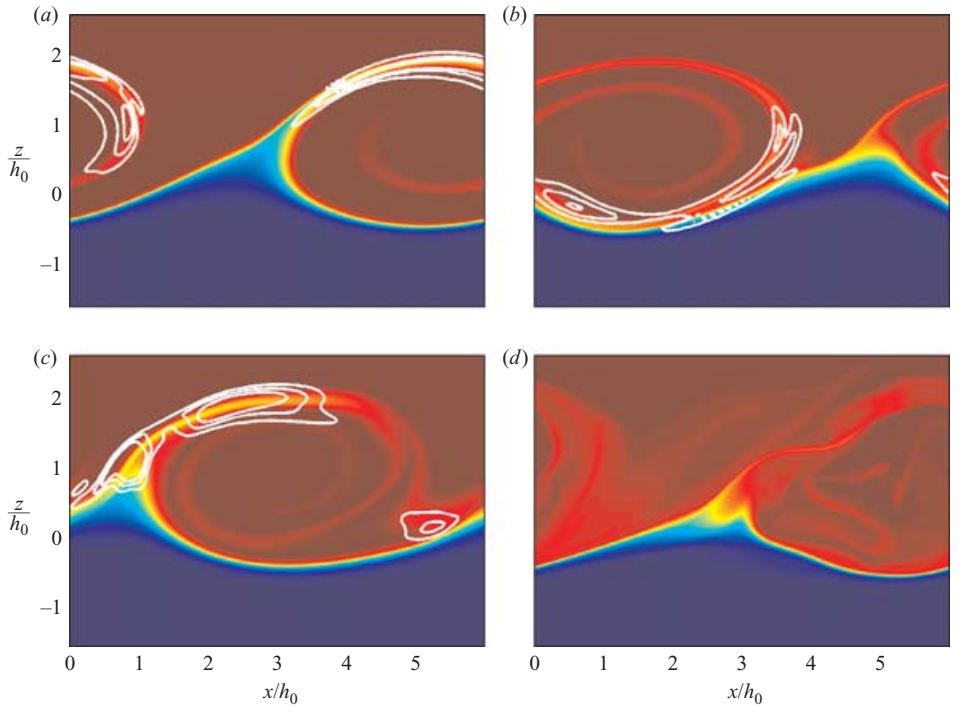

FIGURE 16. Plots of the density field and $\langle \mathscr{K}_{3d} \rangle_y$ contours in the $a = 1.0$ simulation showing times corresponding to the initial development before the sinking of the ejection (a), during the damping phase of $\mathscr{K}_{3d}$ where the ejection has contacted the density interface (b), and during the subsequent growth phase of $\mathscr{K}_{3d}$ as a second ejection is occurring (c). The contours have the values $(1, 2, 3) \times 10^{-7}$ in (a), $(1, 2, 3) \times 10^{-5}$ in (b), and $(3, 5, 7) \times 10^{-5}$ in (c). A time of turbulent motion is shown in (d) without $\langle \mathscr{K}_{3d} \rangle_y$ contours. Slices of the density field in the (x, z)-plane are taken at $y = L_y/2$ with non-dimensional times (a) $t = 30$, (b) $t = 45$, (c) $t = 57$, (d) $= 104$.

underway. The initial stages of this event are visible in the density field of figure 16(c) at a time when $\mathscr{P}$ is very near a local maximum.

Higher rates of mixing are observed in the turbulent phase which is considerably more energetic than the cases of lower asymmetry (as evidenced by the higher levels of ε' in figure 15b). This follows from the greater fraction of shear-layer vorticity available which produces larger billow diameters and higher local Reynolds numbers $Re_L = \Delta u \delta / \nu$, where δ is taken as the billow diameter. The preturbulent period of high $\mathscr{E}_i$ and Γ_i is correspondingly shortened as $\mathscr{K}_{3d}$ grows at a faster rate.

4.2.4. $a > 1$ *cases*

Thus far, as the asymmetry is increased so too are the gains in $\mathscr{P}_B$ and ε'; as the instabilities extract greater energy from the shear layer they are able to produce greater, more energetic mixing. Intuitively, this relationship cannot hold as the asymmetry is increased indefinitely, since the flow would approach the Rayleigh instability of a homogenous free shear layer overlying an undisturbed density interface. In fact, the stability properties of the $a > 1$ modes presented in § 2.2, figure 3, suggest that the resulting instabilities might be closer to that of a Rayleigh mode than a Holmboe mode.

The pairing of adjacent vortices that is present in homogenous and low-J shear layers subject to the Rayleigh and KH instability will be expected to play a role as a increases, and a thorough examination of this mechanism is beyond the scope of the present study. The pairing process in asymmetric flows has been observed by Pawlak & Armi (1998) in their experiments of spatially accelerating stratified shear layers. It should be noted that the mechanism of vortex pairing is not present for the KH simulation discussed above, as confirmed in SW03. At lower J, the pairing of KH billows can have a significant impact on the turbulent transition and the evolution of the flow. Because of these limitations, the $a > 1$ simulations are included to add a level of completeness to the examination of asymmetry effects. Therefore, results of the simulations are not presented in detail here, but will be discussed in the following section in the context of the lower asymmetry simulations.

5. Discussion

It has been found that mixing by shear instabilities can be broken down into two fundamentally different processes that are characteristic of KH and Holmboe-like modes. In the KH case, where the thickness of the density interface is of the same order as the thickness of the shear layer (i.e. $R = 1$), growth of the instability is characterized by a large-scale overturning of the central isopycnal. It is found to have a short, but efficient, preturbulent phase in which the highest rates of mixing are observed. In this state, the saturated KH billow has developed secondary instabilities of large amplitude which supply further energy to the mixing process. This phase ends with the turbulent collapse of the localized unstable regions within the billow core.

In SW03, it was found that the lower primary growth rate of the Holmboe instability led to a longer preturbulent phase where greater mixing was accomplished. Here, a longer preturbulent phase of high-efficiency mixing was found to occur even in the AH instabilities exhibiting larger growth rates. The instability can support more energetic three-dimensional motions before the turbulent transition, leading to greater mixing. It is possible that the importance of the preturbulent phase is particular to the low Re of the flow, since in KH flows with higher Re the greatest rates of mixing are observed in the turbulent phase (Caulfield & Peltier 2000; Staquet 2000).

To compare the growth of three-dimensional motions in each simulation, figure 17(a) shows the evolution of the $\mathscr{K}_{3d}$ reservoir in each case. The $\mathscr{K}_{3d}$ growth of the Holmboe simulation is the result of different processes (Smyth 2007). These include horizontal shear production in the lee of the wave crests as well as sloping convection in the crests of the waves. The ability of AH instabilities to support more energetic three-dimensional motions is indicated by the higher levels of $\mathscr{K}_{3d}$ attained in figure 17(a), and can be attributed to the higher local Reynolds numbers found in these simulations.

Though the properties discussed above apply to all AH instabilities in this study to varying degrees, there are large differences in the total amount of mixing between the various asymmetric cases. The net amount of mixing – measured as the total background potential energy gain due to fluid motions – is plotted for each simulation in figure 17(b). The general trend is the larger the degree of asymmetry becomes, the more the development of the instability is dominated by shear-layer vorticity. In this respect, the larger asymmetries enable extraction of a greater amount of energy from the initial shear layer. This can be seen by looking at the total average kinetic energy reservoir, $\mathscr{K}$, in each of the asymmetric cases shown in figure 17(c). Since the $\mathscr{K}$

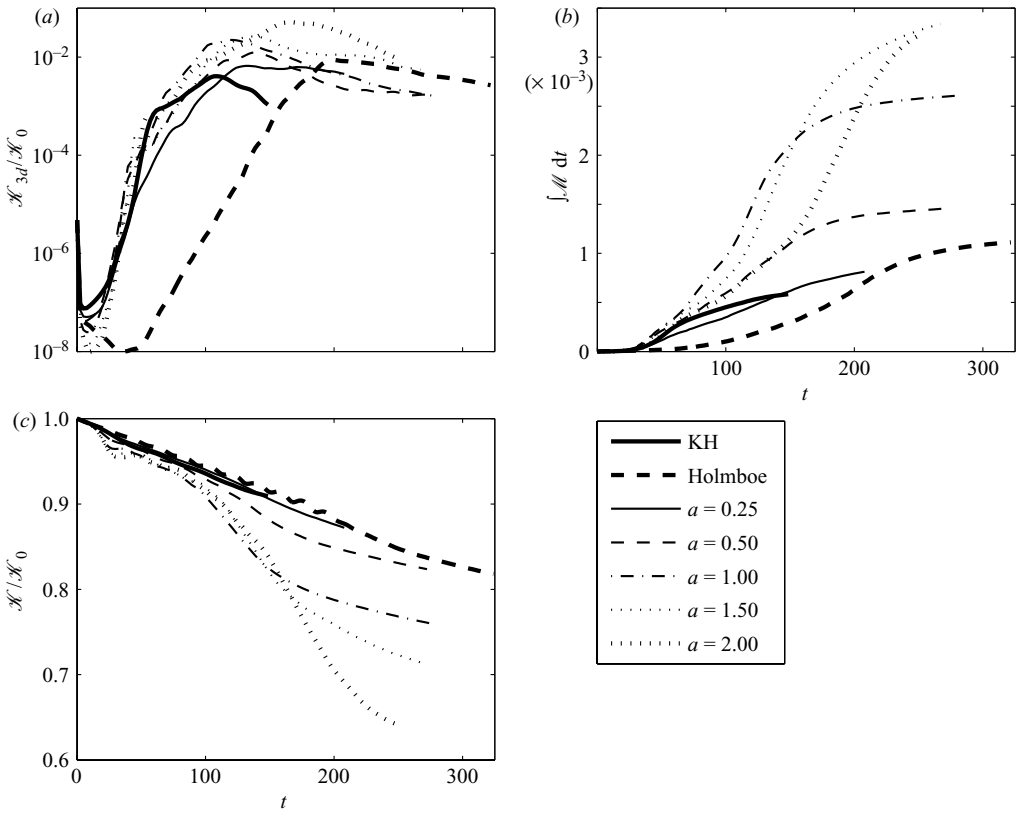

FIGURE 17. Comparison plots for each simulation showing (*a*) $\mathscr{K}_{3d}$, (*b*) the total amount of potential energy gain due to mixing over time, and (*c*) the loss in total kinetic energy $\mathscr{K}$ over time.

reservoir is the energy source of the instability, it gives a good indication of the levels of extraction in each simulation. These plots show a greater extraction of energy as the asymmetry is increased. This result also agrees with the observations of increasing initial billow diameters and an increased presence of ejection events in the cases of greater asymmetry.

Although an increased extraction of energy from the shear layer is observed in cases of greater asymmetry, this does not necessarily lead to a greater mixing of the density field. The proportion of the total energy extracted that is used to perform mixing is given by the cumulative mixing efficiency, $\mathscr{E}_c$. Closely related to this is the cumulative flux coefficient Γ_c, which expresses the ratio of the total amount of energy used to perform mixing to the net amount consumed by the instability and turbulence in the process. Figure 18 shows the net energy gain due to mixing as well as $\mathscr{E}_c$ and Γ_c for various asymmetries. Here it can be seen that increases in a initially lead to a more efficient mixing process. This efficiency begins to drop off for $a \gtrsim 1.5$ and is most probably due to the greater distance between the centre of instability and the density interface. Eventually a point is reached at $a \approx 2$ where although the highest levels of energy are extracted from the shear layer, a similar level of mixing is accomplished. A similar trend can be noted in Γ_c, but it begins to decrease for $a \gtrsim 0.5$. This highlights the shorter durations of the preturbulent mixing phase that occur as higher growth

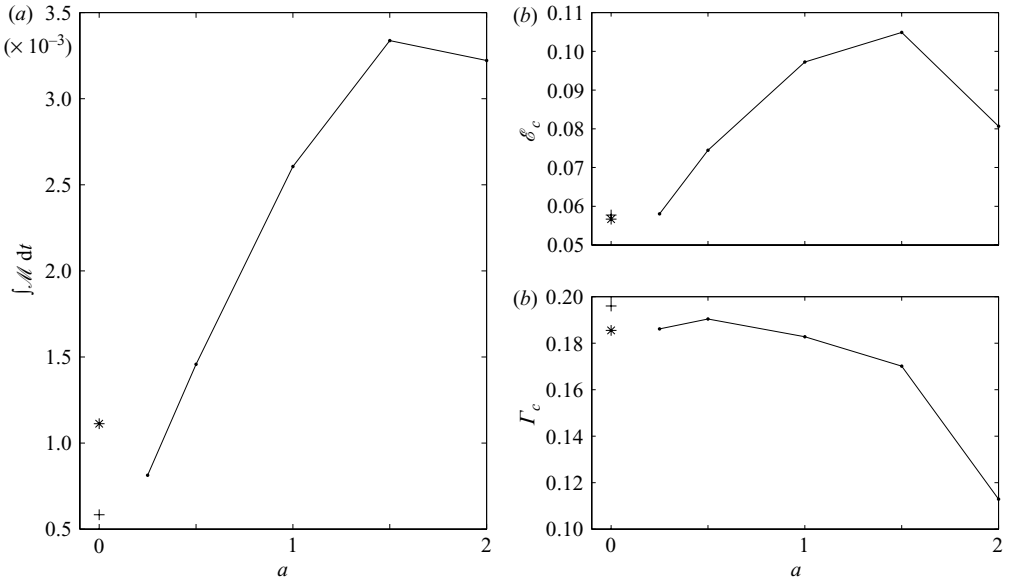

FIGURE 18. Changes in (*a*) the total energy gain due to mixing, (*b*) $\mathscr{E}_c$, and (*c*) Γ_c for the various asymmetries. The cross and asterisk denote values in the KH and Holmboe simulations, respectively.

rates of three-dimensional motion are achieved. The difference in magnitude between the $\mathscr{E}_c$ and the Γ_c measures of efficiency can also be attributed to the role of $\bar{\varepsilon}$ in the denominator of $\mathscr{E}_c$ in (2.15). In flows of higher Re, the $\bar{\varepsilon}$ term can be expected to play a less significant role.

The intuitive notion espoused in SW03 – that for sufficiently large J and R, the density interface effectively acts as a flexible barrier to the vorticity of the shear layer – can be seen to support these results. Since this barrier is sufficiently strong, it prevents communication between layers, and isolates the vorticity of the weaker layer. By this process, the extraction of energy in the AH instability is limited to the shear of the dominant layer until the formation of the weaker mode. As the asymmetry is increased past $a \gtrsim 1.5$, the growth of the instability is increasingly isolated from the density interface and cannot perform mixing as efficiently. Instead, the mixing that is accomplished is mainly through the turbulent entrainment and mixing process that ensues once the transition has taken place. If a were to continue to increase, the instability would approach that of an homogenous shear layer with a vanishing mixing efficiency and flux coefficient.

The simulations having greater asymmetries also show increased levels of mixing in the turbulent phase. With a greater extraction of energy from the shear layer comes larger billow diameters; the largest energy-containing scale of the flow. This feature of AH instabilities allows the local Reynolds numbers attained during the flow evolution to become dependent on the degree of initial asymmetry. It is therefore not surprising that the cases of larger asymmetry show increased mixing during the turbulent phase.

In accordance with the theoretical and laboratory investigation of Lawrence *et al.* (1991), the development of AH instabilities resulted in a distinct one-sidedness. The final result of this one-sidedness is a greater mixing of the density profile in the dominant layer. This can be seen in the final averaged density profiles shown in

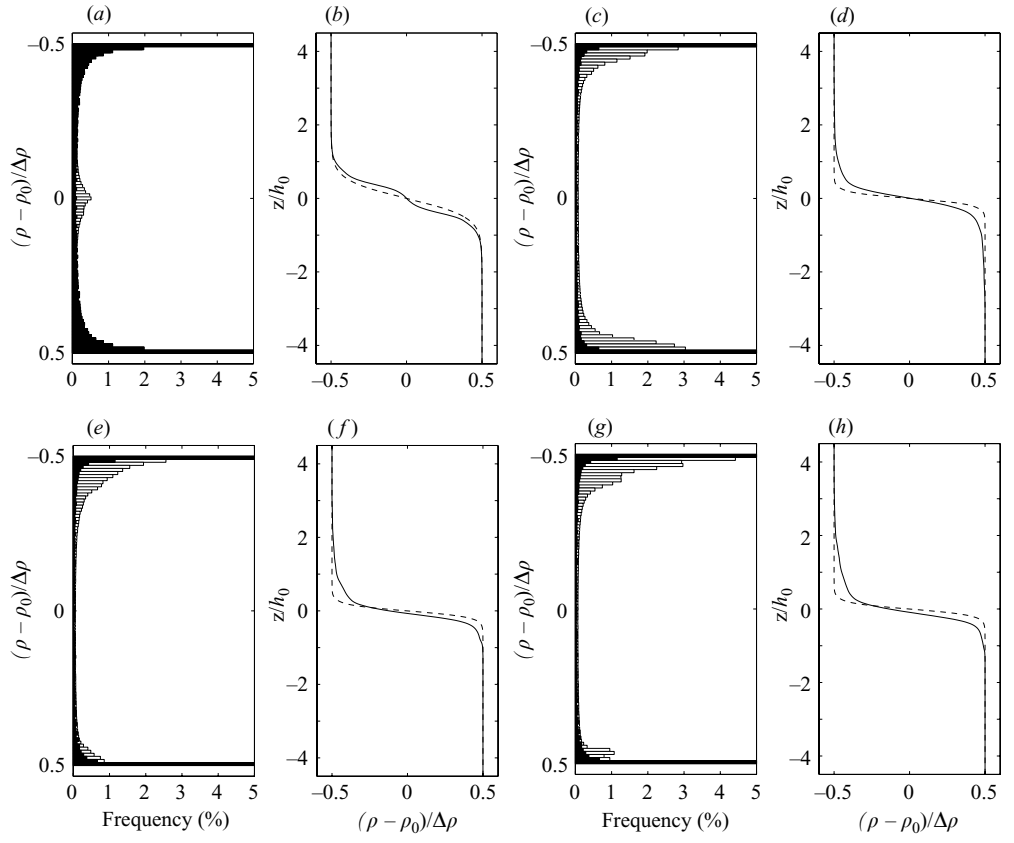

FIGURE 19. Initial and final density characteristics of select simulations. Shown in (*a*), (*c*), (*e*) and (*g*) are the distribution of density elements in the computational domain for the KH, Holmboe, $a = 0.25$ and $a = 0.50$ simulations, respectively. The initial time is denoted by dark bars and the final time by light bars. In (*b*), (*d*), (*f*) and (*h*), the initial (dashed line) and final (solid line) density profiles are given for the KH, Holmboe, $a = 0.25$ and $a = 0.50$ simulations. All density values are given as the difference from the initial mean density ρ_0.

figure 19 where an initial profile is included for comparison. The vertical distribution of density elements is also shown in figure 19 for both an initial and final simulation time. These plots indicate that the mixing processes in AH instabilities are responsible for the production of largely low-density fluid (since the dominant layer coincides with the low-density stream in this case). This confirms the observation that it is fluid from the upper portions of the interface that is mixed in the upper layer. This process results in a slight deepening of the upper layer in which the effects can be noticed at a distance of $\approx 2.5h_0$ from the new interface position. The weaker layer is left relatively untouched with a sharp gradient still intact. This allows for the formation of the weaker mode sometime after the dominant mode has stabilized, as was observed in the $a = 0.25$ and $a = 0.50$ cases.

The different mixing behaviour of the KH instability can also be seen to manifest itself in the final density distribution, shown in figures 19(*a*) and 19(*b*). Here, the mixing process is responsible for producing exclusively intermediate density fluid. This observation was noted in § 4.1 as the mixing was concentrated primarily within

the billow core and originated from the entrainment of high- and low-density fluid from the entire interface into the billow. The increase in intermediate density fluid leaves a step-like structure in the profile with two locations of higher gradients. See Caulfield & Peltier (2000) for a discussion of this density profile generation in KH instabilities of lower J and higher Re. It should also be noted that the vertical extent of the mixing is entirely within the original shear layer and density interface thickness – in marked contrast to the AH cases. The Holmboe simulation (figures 19*c* and 19*d*) displays mixing behaviour similar to the AH cases in that the final density distribution shows mixing concentrated above and below the interface.

The difference between mixing behaviour in AH and Holmboe instabilities and that of KH instabilities was first noticed by Thorpe (1968). While performing tilting-tube experiments, it was observed that in certain mixing events that bear a strong resemblance to the AH instabilities identified here, the density interface 'retains its identity', meaning that mixing is accomplished without the collapse of overturned regions. In this case, there is no mixing of fluid across the interface – as is the dominant process in KH instabilities.

6. Conclusions

A sequence of direct numerical simulations has been performed in which the effects of asymmetry on the evolution and mixing of stratified shear instabilities has been examined. The results are compared to the two symmetric instabilities, namely, the KH and Holmboe instabilities. Two different mixing mechanisms are found to emerge. The first is present only in the KH case, and consists of a large-scale overturning of the central isopycnal. Mixing generated in the collapse of this overturn results in the production of intermediate density fluid, and a layered density profile. The second mixing mechanism is found in both Holmboe and AH instabilities and is characterized by the entrainment of partially mixed fluid from the edge of the interface by a travelling spanwise vortex. This process is marked by periodic ejection events that are initiated during the primary growth of the instability.

High levels of mixing observed in the AH instabilities are the result of a long-lasting efficient preturbulent phase, as well as a greater extraction of energy from the shear layer. The extraction of energy from the shear layer also induces a greater degree of mixing in the longer-lived turbulent phase in cases of high asymmetry. As the level of asymmetry is increased, a greater fraction of the shear-layer vorticity becomes involved in the development of the dominant AH mode, resulting in higher levels of both mixing and viscous dissipation. In cases exhibiting lower asymmetries, the weaker AH mode is found to develop after the turbulent breakdown of the dominant mode. This is only possible because of the one-sided mixing behaviour of the dominant AH mode which leaves the density interface sharp on the side of the weaker layer. As first pointed out by Thorpe (1968), the density interface remains intact during the AH mixing process as a result of this mixing behaviour. The evolution of the flow and additional mixing associated with the weaker mode has not been studied in detail.

Three-dimensional structure in the dominant AH modes was found to consist of streamwise vortical structures that appear to have their origins in the locally unstable density regions that develop. These structures are influenced by the periodic ejections of fluid from the cusp region, and are similar to those observed in the laboratory experiments of Schowalter *et al.* (1994). The interaction of the streamwise vortices with

the density interface – particularly during the sinking of ejections to the interface level – was found to influence the growth of the kinetic energy of the secondary structures. The analysis of secondary structure presented does not constitute a rigorous proof of the mechanisms involved however, and must be left for another study. These processes have further implications for the turbulent transition in AH instabilities that have not been fully quantified.

Consideration of the features mentioned above have led to the conclusion that the degree of asymmetry present in the velocity and density profiles is an important factor in the mixing of stratified shear flows. However, the study of asymmetry in these flows is far from complete. The present study has focused entirely on a single point in parameter space, and is representative of only very low-Re mixing events from a geophysical perspective. A more thorough examination would include a number of points throughout the bulk Richardson number domain as well as exploring Reynolds number effects.

Funding and support provided by the Natural Sciences and Engineering Research Council of Canada, the Canada Research Chairs Program, and the National Science Foundation (USA, OCE 0221057) is gratefully acknowledged. The computational resources required for this study were provided by WestGrid.

REFERENCES

Alexakis, A. 2005 On Holmboe's instability for smooth shear and density profiles. *Phys. Fluids* **17**, 84–103.

Armi, L. & Farmer, D. 1988 The flow of Mediterranean water through the strait of Gibraltar. *Prog. Oceanogr.* **21**, 1–98.

Baines, P. G. & Mitsudera, H. 1994 On the mechanism of shear flow instabilities. *J. Fluid Mech.* **276**, 327–342.

Batchelor, G. 1959 Small-scale variation of convected quantities like temperature in turbulent fluid. *J. Fluid Mech.* **5**, 113–133.

Caulfield, C. P. & Peltier, W. R. 1994 Three dimensionalization of the stratified mixing layer. *Phys. Fluids* **6**, 3803–3805.

Caulfield, C. P. & Peltier, W. R. 2000 Anatomy of the mixing transition in homogenous and stratified free shear layers. *J. Fluid Mech.* **413**, 1–47.

Cortesi, A. B., Yadigaroglu, G. & Bannerjee, S. 1998 Numerical investigation of the formation of three-dimensional structures in stably stratified mixing layers. *Phys. Fluids* **10**, 1449–1473.

Dimotakis, P. E. 2000 The mixing transition in turbulent flows. *J. Fluid Mech.* **409**, 69–98.

Dimotakis, P. E. 2005 Turbulent mixing. *Annu. Rev. Fluid Mech.* **37**, 329–356.

Haigh, S. P. 1995 Non-symmetric Holmboe waves. PhD thesis, University of British Columbia.

Haigh, S. P. & Lawrence, G. A. 1999 Symmetric and nonsymmetric Holmboe instabilities in an inviscid flow. *Phys. Fluids* A **11**, 1459–1468.

Hazel, P. 1972 Numerical studies of the stability of inviscid parallel shear flows. *J. Fluid Mech.* **39**, 39–61.

Hogg, A. M. & Ivey, G. N. 2003 The Kelvin–Helmholtz to Holmboe instability transition in stratified exchange flows. *J. Fluid Mech.* **477**, 339–362.

Holmboe, J. 1962 On the behaviour of symmetric waves in stratified shear layers. *Geofys. Publ.* **24**, 67–112.

Howard, L. N. 1961 Note on a paper of John W. Miles. *J. Fluid Mech.* **10**, 509–512.

Ivey, G. N. 2004 Stratification and mixing in sea straits. *Deep-Sea Res. II* **51**, 451–453.

Klaassen, G. & Peltier, W. R. 1991 The influence of stratification on secondary instability in free shear layers. *J. Fluid Mech.* **227**, 71–106.

Lawrence, G. A., Browand, F. K. & Redekopp, L. G. 1991 The stability of a sheared density interface. *Phys. Fluids* A **3**, 2360–2370.

Lawrence, G. A., Haigh, S. P. & Zhu, Z. 1998 In search of Holmboe's instability. In *Physical Processes in Lakes and Oceans* (ed. J. Imberger). Coastal and Estuarine Studies, vol. 54, pp. 295–304. American Geophysical Union.

Maxworthy, T. & Browand, F. K. 1975 Experiments in rotating and stratified flows: oceanographic application. *Annu. Rev. Fluid Mech.* **7**, 273–305.

Miles, J. W. 1961 On the stability of heterogeneous shear flows. *J. Fluid Mech.* **10**, 496–508.

Moin, P. & Mahesh, K. 1998 Direct numerical simulation: a tool in turbulence research. *Annu. Rev. Fluid Mech.* **30**, 539–578.

Pawlak, G. & Armi, L. 1998 Vortex dynamics in a spatially accelerating shear layer. *J. Fluid Mech.* **376**, 1–35.

Peltier, W. R. & Caulfield, C. P. 2003 Mixing efficiency in stratified shear flows. *Annu. Rev. Fluid Mech.* **35**, 135–167.

Rayleigh, Lord 1880 On the stability, or instability, of certain fluid motions. *Proc. Lond. Math. Soc.* **12**, 57–70.

Sargent, F. E. & Jirka, G. H. 1987 Experiments on saline wedge. *J. Hydraul. Engng ASCE* **113**, 1307–1324.

Schowalter, D. G., Van Atta, C. W. & Lasheras, J. C. 1994 A study of streamwise vortex structure in a stratified shear layer. *J. Fluid Mech.* **281**, 247–291.

Scinocca, J. F. 1995 The mixing of mass and momentum by Kelvin–Helmholtz billows. *J. Atmos. Sci.* **52**, 2509–2530.

Smyth, W. D. 1999 Dissipation range geometry and scalar spectra in sheared, stratified turbulence. *J. Fluid Mech.* **401**, 209–242.

Smyth, W. D. 2007 Secondary circulations in Holmboe waves. *Phys. Fluids* **18**, 064104.

Smyth, W. D. & Moum, J. N. 2000*a* Length scales of turbulence in stably stratified mixing layers. *Phys. Fluids* **12**, 1327–1342.

Smyth, W. D. & Moum, J. N. 2000*b* Anisotropy of turbulence in stably stratified mixing layers. *Phys. Fluids* **12**, 1343–1362.

Smyth, W. D. & Peltier, W. R. 1990 Three-dimensional primary instabilities of a stratified, dissipative, parallel flow. *Geophys. Astrophys. Fluid Dyn.* **52**, 249–261.

Smyth, W. D. & Winters, K. B. 2003 Turbulence and mixing in Holmboe waves. *J. Phys. Oceanogr.* **33**, 694–711.

Smyth, W. D., Klaassen, G. P. & Peltier, W. R. 1988 Finite amplitude Holmboe waves. *Geophys. Astrophys. Fluid Dyn.* **43**, 181–222.

Smyth, W. D., Moum, J. N. & Caldwell, D. R. 2001 The efficiency of mixing in turbulent patches: inferences from direct simulations and microstructure observations. *J. Phys. Oceanogr.* **31**, 1969–1992.

Smyth, W. D., Nash, J. D. & Moum, J. N. 2005 Differential diffusion in breaking Kelvin–Helmholtz billows. *J. Phys. Oceanogr.* **35**, 1004–1022.

Smyth, W. D., Carpenter, J. R. & Lawrence, G. A. 2007 Mixing in symmetric Holmboe waves. *J. Phys. Oceanogr.* in press.

Staquet, C. 2000 Mixing in a stably stratified shear layer: two- and three-dimensional numerical experiments. *Fluid Dyn. Res.* **27**, 367–404.

Thorpe, S. A. 1968 A method of producing a shear flow in a stratified fluid. *J. Fluid Mech.* **32**, 693–704.

Thorpe, S. A. 1973 Experiments on instability and turbulence in stratified shear flow. *J. Fluid Mech.* **61**, 731–751.

Thorpe, S. A. 1985 Laboratory observations of secondary structures in Kelvin–Helmholtz billows and consequences for ocean mixing. *Geophys. Astrophys. Fluid Dyn.* **34**, 175–199.

Thorpe, S. A. 1987 Transitional phenomena and the development of turbulence in stratified fluids: a review. *J. Geophys. Res.* **92C**, 5231–5248.

Winters, K. B. & Seim, H. E. 2000 The role of dissipation and mixing in exchange flow through a contracting channel. *J. Fluid Mech.* **407**, 265–290.

Winters, K B., Lombard, P. N., Riley, J. J. & D'Asaro, E. A. 1995 Available potential energy and mixing in density-stratified fluids. *J. Fluid Mech.* **289**, 115–128.

Winters, K. B., MacKinnon, J. A. & Mills, B. 2004 A spectral model for process studies of rotating, density-stratified flows. *J. Atmos. Ocean. Tech.* **21**, 69–94.

Woods, J. D. 1968 Wave-induced shear instability in the summer thermocline. *J. Fluid Mech.* **32**, 791–800.

Yonemitsu, N., Swaters, G. E., Rajaratnam, N. & Lawrence, G. A. 1996 Shear instabilities in arrested salt-wedge flows. *Dyn. Atmos. Oceans* **24**, 173–182.

Yoshida, S., Ohtani, M., Nishida, S. & Linden, P. F. 1998 Mixing processes in a highly stratified river. In *Physical Processes in Lakes and Oceans* (ed. J. Imberger). Coastal and Estuarine Studies, vol. 54, pp. 389–400. American Geophysical Union.